Naval Research Laboratory

Stennis Space Center, MS 39529-5004

NRL/FR/7330--02-10,036

Anatomy of the Ocean Surface Roughness

PAUL A. HWANG
DAVID W. WANG
WILLIAM J. TEAGUE
GREGG A. JACOBS
JOEL WESSON

Ocean Sciences Branch
Oceanography Division

DEREK BURRAGE

University of Southern Mississippi
Stennis Space Center, MS

JERRY MILLER

Office of Naval Research
International Field Office
London NW1 5TH, United Kingdom

December 31, 2002

REPORT DOCUMENTATION PAGE

Form Approved
OMB No. 0704-0188

1. REPORT DATE *(DD-MM-YYYY)*	**2. REPORT TYPE**	**3. DATES COVERED** *(From - To)*
31-12-2002	Formal	

4. TITLE AND SUBTITLE

Anatomy of the Ocean Surface Roughness

5a. CONTRACT NUMBER

5b. GRANT NUMBER

5c. PROGRAM ELEMENT NUMBER
61153N

6. AUTHOR(S)

Paul A. Hwang, David W. Wang, William J. Teague, Gregg A. Jacobs,
Joel Wesson, Derek Burrage,* and Jerry Miller**

5d. PROJECT NUMBER

5e. TASK NUMBER

5f. WORK UNIT NUMBER
8206-02, 8190-02

7. PERFORMING ORGANIZATION NAME(S) AND ADDRESS(ES)

Naval Research Laboratory
Stennis Space Center, MS 39529-5004

8. PERFORMING ORGANIZATION REPORT NUMBER

NRL/FR/7330--02-10,036

9. SPONSORING / MONITORING AGENCY NAME(S) AND ADDRESS(ES)

Office of Naval Research
800 N. Quincy St.
Arlington, VA 22217-5660

10. SPONSOR / MONITOR'S ACRONYM(S)

11. SPONSOR / MONITOR'S REPORT NUMBER(S)

12. DISTRIBUTION / AVAILABILITY STATEMENT

Approved for public release; distribution is unlimited.

13. SUPPLEMENTARY NOTES

* University of Southern Mississippi, Stennis Space Center, MS 39529
** Office of Naval Research, International Field Office, London NW1 5TH, United Kingdom

14. ABSTRACT

Ocean surface roughness can be decomposed into an ambient component, surface wave geometric contribution (the mean square slope), and breaking wave contribution (the breaking roughness). Only the last two components can be attributed to local wind conditions for remote sensing considerations. The ambient roughness level is estimated to be about 0.01 from altimeter data. The rate of increase of breaking roughness with wind speed is much faster than the counterpart of the mean square slope of wave geometry. In high wind conditions, the breaking roughness contribution may exceed the wind-wave geometrical contribution. Data collected in clean and slick conditions and newer data of filtered surface roughness derived from spaceborne altimeters are analyzed to provide a quantitative description of the breaking roughness. Application of the refined understanding of surface roughness to improve wind speed retrieval from altimeter data is described.

15. SUBJECT TERMS

Altimeter	Ambient roughness	Breaking roughness	Mean square slope
Ocean surface roughness	Remote sensing	Scattering cross section	Wave spectrum

16. SECURITY CLASSIFICATION OF:			**17. LIMITATION OF ABSTRACT**	**18. NUMBER OF PAGES**	**19a. NAME OF RESPONSIBLE PERSON**
a. REPORT	**b. ABSTRACT**	**c. THIS PAGE**			Paul A. Hwang
Unclassified	Unclassified	Unclassified	SAR	45	**19b. TELEPHONE NUMBER** *(include area code)* 228-688-4708

Standard Form 298 (Rev. 8-98)
Prescribed by ANSI Std. Z39.18

CONTENTS

ANATOMY OF THE OCEAN SURFACE ROUGHNESS

1. INTRODUCTION

The properties of the ocean surface roughness control many dynamical and mechanical processes occurring at the air-sea interface. Examples include air-sea mass, momentum and energy exchanges and electromagnetic or acoustic wave scattering from above or below the ocean surface. In many applications, ocean surface roughness has been equated with the mean square slopes (mss) of wind waves. This concept has led to difficulties in explaining field observation of roughness-related phenomena such as surface wind stress and radar scattering from the ocean surface. Due to the lack of clear understanding of ocean surface physics, in some applications the role of roughness is seriously distorted or completely ignored. For example, in the derivation of wind speed from altimeter or scatterometer output, operational algorithms rely on empirical relations established from correlating collocated and simultaneous datasets of in situ wind speeds and backscattering cross sections. The physics of wind generation of waves and scattering of radar waves from surface roughness produced by ocean wave undulation are totally avoided. With the empirical approach described above, there is little room for improvement in the accuracy of the derived geophysical parameters (e.g., wind speed from altimeter and scatterometer, salinity from microwave emission) even when major enhancements in sensor hardware and software have been implemented.

The purpose of this report is to summarize the results from our recent investigation of the physical characteristics of ocean surface roughness and to relate that understanding to the derivation of geophysical parameters at the air-sea interface. In particular, our recent analysis of spaceborne altimeter scattering cross sections and the mean square slope data from the ocean surface has led us to conclude that there are at least three roughness components: the mean square slope of wind-generated waves (wave geometry), ambient roughness (turbulence and swell, not related to local wind), and breaking roughness (which must be distinguished from wave geometry). Quantification of the surface roughness, especially the spatial properties of these various components, will significantly enhance our understanding of the mechanisms of air-sea exchange and processes of ocean remote sensing. This report presents an attempt to provide a quantitative description of the various components. Section 2 revisits the classical dataset of Cox and Munk (1954) on ocean surface roughness. The dataset is comprised of two major groups with 23 data points collected in clean water conditions and 9 data points in slicked water conditions. It is worthwhile to point out that while analytically the slicked data subset can be explained by the saturation spectrum (Phillips 1966; Hwang and Wang 2001), the interpretation of the clean water subset is less certain and spectral models created to match the observed clean water data subset differ in significant ways. It is quite interesting to note that despite the lack of a comprehensive agreement on the surface spectral properties producing the observed clean water results, those observations are much more widely cited than are the slicked results.

In order to find an explanation of the big difference between the slicked and clean water cases, spaceborne altimeter data are studied. The altimeter data share many common attributes with the Sun glitter data of Cox and Munk (1954), collected mostly around noon time. The altimeter dataset has the advantage of using an active system, therefore the source of electromagnetic scatter and the cutoff wavelength of system are well defined. Earlier attempts to retrieve the mean square roughness from altimeter data cannot be considered successful because the resulting roughness derived from radar data is

Manuscript approved July 30, 2002.

found to be larger than that from optical sensing, a very unreasonable result as pointed out by Hwang (1997) and further explained as due to the failure to account for the ambient surface roughness in the ocean. With the improved understanding, an algorithm to retrieve the wind-induced surface roughness is developed. The roughness derived from altimeter data is also much larger than that which can be explained by the combined equilibrium and saturation spectrum (Hwang and Wang 2001). A hypothesis is put forth that the large difference is due to surface wave breaking that makes abnormally large contributions to electromagnetic scatters (sea spikes). This hypothesis seems to receive some support from the physical description by Cox and Munk (1954) on the coherence structure of the slicks they laid out. This suggests that the surface slick suppressed not only short waves but also breaking events.

To further investigate the properties of ambient roughness, collocated and simultaneous buoy and altimeter measurements from the Gulf of Alaska, Bering Sea, and the Hawaiian Islands regions are analyzed in Section 3. The derived ambient roughness shows some minor dependence on wind speed and wave height. An empirical function is proposed based on best agreement of the calculated and measured altimeter cross sections.

The improved knowledge of surface roughness components is put in use to develop a wind speed retrieval algorithm based on the physics of altimeter scattering from a rough ocean surface. The physics-based equation produces a wind speed product that compares very well with the best operational algorithm of modified Chelton and Wentz (MCW, Witter and Chelton 1991). Section 4 provides further detail.

From the analysis presented, it is concluded in Section 5 that we need to discard the current practice of equating the ocean surface roughness with the mean square slope. In addition to the mean square surface wave geometry, ambient roughness exists in the absence of wind-generated waves in the ocean. The average level of the ambient roughness is about 0.008. The main source of the ambient roughness is probably not ocean swell but turbulence in the omnipresent currents. The effects of breaking on electromagnetic scattering are much stronger than the effect on modifying the ocean wave spectrum. Interpreting breaking contribution in the electromagnetic signals as equivalent to mean square slope of ocean waves will lead to unrealistic ocean wave spectral models.

2. OCEAN SURFACE ROUGHNESS COMPONENTS

2.1 Background

Collecting in situ measurements of the surface roughness is a difficult task in the ocean. Interestingly, with all the technical advances over the last half century, the milestone work of the airborne measurements of Sun glitter conducted in 1951 by Cox and Munk (1954, referred to herein as CM) remains the most comprehensive among all the experiments reporting the mean square slope data. In their paper, two series of experiments are reported, one on clean water surfaces and the other with natural or artificial slicks that effectively suppressed short waves and provided the low-pass filtered roughness of the ocean surface. CM calculate the damping factor of the slicks used in their experiments and conclude that the filtered wavelength is 0.3 m. For the clean surface series, the wind speed range is from 0.7 to 13.5 m s^{-1}; for the slick surface series, the wind speed range is from 1.6 to 10.6 m s^{-1}. These data have served as a major calibration reference in many areas of research, ranging from air-sea interaction and wave dynamics to acoustic and electromagnetic remote sensing applications.

The logarithmic wind speed dependence of the CM slick data is in good agreement with the analytical prediction of the mean square slope calculated with a saturation spectrum (Phillips 1966). Starting in the 1970s, the equilibrium spectral function is recognized to be more representative of the wind-generated waves (e.g., Toba 1978; Phillips 1985; Hwang et al. 2000). Recent comparison of the CM slick data with the mean square slope of an equilibrium/saturation spectral function also shows satisfactory agreement (Hwang and Wang 2001). In contrast, the linear wind speed dependence of the CM clean surface data remains difficult to explain. If the difference between the clean surface and slick surface data is a matter of extending the saturation spectrum to a higher wavenumber, the resulting logarithmic extension

significantly underestimates the clean water data at medium-to-high wind speeds. A quantitative discussion is presented in Section 2.2.

Over the years, spaceborne altimeters such as GEOSAT and TOPEX/POSEIDON have produced high quality scattering cross section measurements in the world oceans. The radar cross section is closely related to the sea surface roughness. In fact, the derivation of wind speeds from radar measurements is based on the dual correlations of radar cross-section with surface roughness and the surface roughness with wind speed. Section 2.3 describes the procedure to retrieve the wind-induced roughness component from the altimeter cross section. Collocated data of altimeter and buoy measurements are acquired from the Bering Sea, Gulf of Alaska, and the Hawaiian regions. The data from these regions cover a wide range of wind speeds (0 to 20 m s^{-1}) and sea states (0 to 9 m significant wave heights). Section 2.4 describes these datasets.

Similar to the measurement in slick covered surfaces, the roughness measured by radar also represents a low-pass filtered roughness with the filtered length scale in proportion to the radar wavelength. For Ku-band (13.6 GHz), the radar wavelength is 0.022 m. Using the commonly cited value of 3 as the proportionality factor (e.g., Jackson et al. 1992), the altimeter data represent surface roughness low-passed at 0.066 m. The altimeter measurements thus exclude the difficult region of capillary-gravity (CG) wave contribution. The spectral properties of CG waves remain largely uncertain in medium-to-high wind speeds (further discussed in Section 2.6). The main result from the analysis of altimeter data is that the derived wind-induced filtered roughness is considerably higher than the filtered mean square slope calculated from the equilibrium/saturation spectrum, a conclusion similar to that derived from the comparison of the CM clean and slick measurements. The filtering operation of altimeter measurements is fundamentally the same as slick suppression of short waves. However, there is a major difference: the altimeter sensing does not alter the sea surface condition. Based on CM's description that the slick surfaces remain *coherent* in conditions of less than 20 mph (about 9 m s^{-1}), it is likely that the oil slicks they have laid on the surface suppressed not only short waves but also the wave breaking. Here, it is suggested that the large difference between wind-induced roughness of the clean surface (either from Sun glitter data or altimeter filtered measurements) and the mean square slope calculated from the wave spectrum is contributed by breaking waves (Hwang 2002). This roughness difference is referred to as the breaking roughness in this report. The data show that the breaking roughness increases with wind speed following a power-law function with the exponent of power-law equal to 1.5. The wind speed at which breaking roughness becomes apparent is 3.5 m s^{-1}. Sections 2.5 and 2.6 present the details of the results and discussions, and Section 2.7 provides a summary.

2.2 Roughness of Clean and Slick Surfaces

The mean square slope results reported by CM are derived from analyzing the sun glitter patterns of the ocean surface obtained from an aircraft flying at an altitude of about 600 m. The area of coverage for each image of glitter patterns is typically on the order of one-half square kilometer. The results, therefore, yield a high degree of statistical confidence. These data are shown in Fig. 1(a). Based on these measurements, CM report that the mean square slope s of the ocean surface increases linearly with wind speed, and the following two formulas are given:

$$s_{clean} = 5.12 \times 10^{-3} U + (3 \pm 4) \times 10^{-3}, \text{ for a clean surface,} \tag{1}$$

and

$$s_{slick} = 1.56 \times 10^{-3} U + (8 \pm 4) \times 10^{-3}, \text{ for a slick surface.} \tag{2}$$

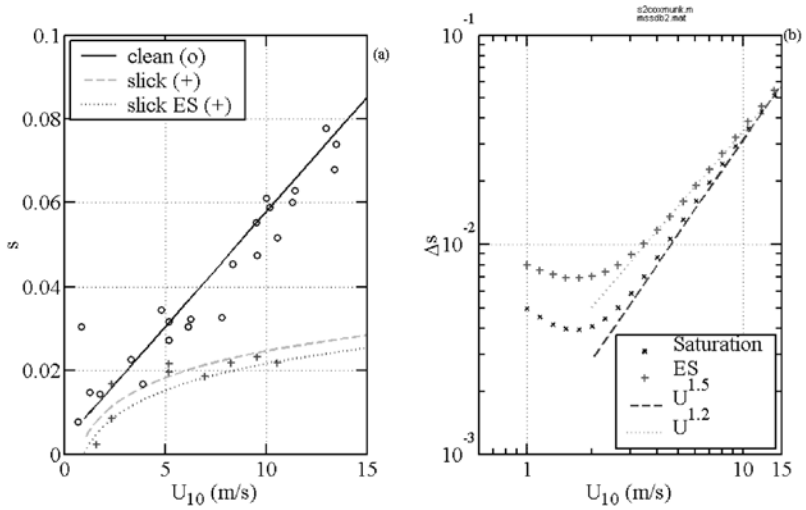

Fig. 1 — (a) Mean square slopes reported by Cox and Munk (1954). The dashed curve is the logarithmic increase expected from the saturation spectrum (Eq. (3)), the dotted curve is from the saturation and equilibrium spectra (Eq. (4)). The solid line is the linear wind speed relation fitted through the clean water data (Eq. (5)); (b) The difference of the roughness between clean surface and slick surface measurements calculated with saturation spectrum (crosses) and equilibrium/ saturation spectrum (pluses). The slopes of the dashed and dotted curves are 1.5 and 1.2, respectively.

In Eqs. (1) and (2), the wind velocity, U, is measured at a 12.5-m elevation. At medium to high wind speeds, the wind-induced roughness on a clean surface is two to three times larger than that on a slick surface.

CM compare the measured mean square slopes with calculations using the Darbyshire and Neumann wave spectra. They found reasonable agreement in the slick data but the large difference between the clean surface and slick data cannot be explained by extrapolating the spectral function from the slick cutoff wavenumber k_s into the capillary region (pp. 218-222, CM). Our understanding of the wave spectral function has evolved significantly since the 1950s. Phillips (1966) recalculates the mean square slopes of slick covered cases using the saturation spectral function (Phillips 1958). Because waves longer than the peak wavelength make only insignificant contribution to the surface slope, the total mean square slope can be computed from the peak wavenumber to the cutoff wavenumber of slick suppression. The result shows that the mean square slopes of slick cases increase logarithmically with wind speed,

$$s_s = B \ln\left(\frac{k_s U_{10}^2}{g}\right), \tag{3}$$

where k_s is the cutoff wavenumber of slick suppression and g is the gravitational acceleration. Equation (3) with $B = 4.6 \times 10^{-3}$, shown as the dashed curve in Fig. 1(a), is in better agreement with the field data than the linear function originally proposed by CM. More recently, the equilibrium spectral function is considered a more accurate representation of the wave spectrum, especially in the region close to the spectral peak (e.g., Toba 1978; Phillips 1985; Hwang et al. 2000). Hwang and Wang (2001) analyze the mean square slopes computed from the equilibrium and saturation spectral ranges and the agreement with the slick data remains very good:

$$s_{es} = \left[2bC_d^{0.5}\left(m^{0.5} - 1\right) - B\ln m\right] + B\ln\left(\frac{k_c U_{10}^{\ 2}}{g}\right), \tag{4}$$

where k_c is the cutoff wavenumber, equal to k_s for the slick data, and $2\pi/\lambda_c$ for radar data discussed in

Section 2.5, $m = k_i/k_p$, representing the ratio of the separation wavenumber k_i between the equilibrium and saturation ranges. The numerical value of m is calculated to be in the neighborhood of 6.5 ± 2.5.The other coefficients are the dimensionless spectral coefficients at saturation (B) and equilibrium (b): $B = 4.6 \times 10^{-3}$, $b = 5.2 \times 10^{-2}$, and the drag coefficient $C_d = 1.2 \times 10^{-3}$. More detailed discussion of the results of mean square slopes based on this spectral representation and the comparison with the slick measurements by Cox and Munk (1954) are given by Hwang and Wang (2001). The difference between Eqs. (4) and (3) is the square bracketed term on the right-hand side of Eq. (4). The magnitude of the term is -2.99×10^{-3} (Table 1, Hwang and Wang 2001), which is small and within the uncertainty of the CM measurements. It can be concluded from these analyses that the surface roughness in slick conditions is primarily the mean square slopes of the local wind-generated waves.

While the progress made in the understanding of the wave spectrum has provided incremental improvement in our knowledge of the surface roughness measured from slick covered ocean surfaces, the cause of the large increase of the roughness measured in clean surface conditions remains unknown. This situation is not satisfactory since in most applications such as remote sensing and air-sea interaction, the ocean surface is less likely to be covered with slicks. An understanding of the wind-induced roughness properties on a clean surface, especially the source of the large enhancement of surface roughness above the mean square slope calculated from the wave spectrum, will have great benefits toward improving our knowledge of air-sea transfer processes and remote sensing of the ocean. Without a better understanding of the physical processes contributing to the enhanced roughness of the clean surface condition, the empirical linear wind speed relationship will be retained in the following discussion, except that U (measured at 12.5 m) is replaced by U_{10}, which increases the coefficient in Eq. (1) by approximately 6 percent,

$$s_{clean} = 5.43 \times 10^{-3} U_{10} + 3 \times 10^{-3}, \text{ for a clean surface.} \tag{5}$$

The solid curve in Fig. 1(a) represents the calculation using Eq. (5).

Extending the saturation spectrum into high wavenumbers only produces a logarithmic increase of the mean square slope (Eqs. (3) and (4)). The roughness difference Δs observed between the clean and slick surface conditions displays a much higher rate of increase with wind than the logarithmic growth of the mean square slope of surface waves. Figure 1(b) plots $\Delta s(U_{10})$ computed from Eq. (5) minus Eq. (4) and Eq. (5) minus Eq. (3). The rate of increase with wind follows a power-law function at medium-to-high wind speeds. The exponent is between 1.2 to 1.5 for U_{10}>3 m s^{-1}. The contribution of CG waves has been suggested to explain the roughness difference between clean and slick cases. Recent field data of the CG wave spectrum seem to indicate linear wind speed dependence on the CG wave spectral density. This subject is discussed further in Section 2.6.

2.3 Ambient Roughness: Key to Retrieving Roughness from Altimeter Scattering Cross Section

Over the years, spaceborne altimeters have produced high quality scattering cross-section measurements in the world's oceans. The altimeter backscattering cross section σ_0 is related to the ocean surface roughness by (e.g., Barrick 1968; Brown 1978)

$$\sigma_0 = \frac{R_0}{s_r}, \tag{6}$$

where R_0 is the Fresnel reflection coefficient for normal incidence, and s_r is the total filtered surface roughness contributing to altimeter backscatter. From this relation, ocean surface roughness can be derived from altimeter cross section and wind speed output from collocated ocean buoys.

Hwang (1997) presents a review of the mean square slopes derived from the ocean environment. It is shown that when comparing the mean square surface slopes derived from altimeters and in situ optical sensors, the mean square slopes derived from altimeters persistently exceed those measured by optical sensors for the same wind speed. This is a rather unreasonable outcome, as the radar wavelength is a few orders of magnitude longer than the optical wavelength, therefore, the radar responds to only a smaller fraction of the total roughness (low-passed by the wavelength) as compared to the optical sensors. In other words, the same surface (for a given wind speed) should appear smoother to the radar than to the optical instrument. Hwang et al. (1998) suggest that in the open ocean, ambient roughness is almost always present. Such roughness is not related to the local wind event and needs to be taken into consideration in interpreting the altimeter measurements. It is shown that significant improvement between calculated and measured cross sections can be achieved when the surface roughness is represented by

$$s_r = s_w + S, \tag{7}$$

where S is an ambient roughness component and s_w is the contribution from local-wind-generation (Hwang et al. 1998 and Section 3). Equation (6) becomes

$$\sigma_0 = \frac{R_0}{s_w + S}. \tag{8}$$

Evidence supporting this roughness decomposition is found in the satisfactory explanation of the data scatter of the cross-section measurements as a function of wind speed and the improved agreement between measurements and analytical computations when the ambient roughness is considered. More detailed discussions are presented in Section 3. The analysis indicates that altimeter scattering from the ocean surface needs to be considered as a multiple-input process. In particular, if each additional process adds roughness to the ocean surface, it is the upper bound of $\sigma_0(U_{10})$, not the average over wind speed bins as in general practice, that can provide the information of the local-wind-induced surface roughness. Denoting σ_{0u} as the upper bound of $\sigma_0(U_{10})$, then

$$s_w = \frac{R_0}{\sigma_{0u}}. \tag{9}$$

2.4 Collocated Altimeter and Buoy Datasets

Collocated wind and wave data from NDBC (National Data Buoy Center) buoys and TOPEX groundtracks are collected from two regions with distinctive wind and wave conditions, Gulf of Alaska and Bering Sea (referred to as GoA hereafter) and Hawaiian Islands (referred to as Hawaii hereafter). The maximum time and space differences between buoy locations and altimeter footprints are set to be 0.5 h and 100 km. Detailed information on processing of the merged buoy and altimeter datasets have been presented in Hwang et al. (1998) and will not be repeated here. Table 1 lists the buoy stations and satellite track numbers used here. Most of the buoys are operational over the 7 years of the TOPEX data (1992 to 1999) analyzed in this report.

Table 1 — Buoy Stations and Satellite Tracks in the Two Regions Selected for this Study

NDBC Buoy ID	Buoy Location	TOPEX Tracks	Region
46001	(56°17'44"N 148°10'19"W)	11, 27	Gulf of Alaska
46003	(51°49'53"N 155°51'01"W)	91, 100	
46035	(56°54'38"N 177°48'38" W)	28,101	Bering Sea
51001	(23°24'04"N 162°15'59" W)	36, 92	Hawaiian Islands
51002	(17°10'12"N 157°48'24"W)	3, 23	
51003	(19°10'17"N 160°43'47" W)	92	
51004	(17°26'12" N 152°31'10" W)	79, 99	

In the raw dataset, some large scattering cross sections are due to the deficiency in the altimeter waveform algorithm in treating specular returns from very calm surfaces (E. Walsh and D. Vandemark, private communication, 2000). These data are found to correlate with high attitude angles of the altimeter outputs. Two steps are done in the preprocessing of the data. First, data points with attitude angles greater than 0.3° and σ_0>20 dB are removed (2.43 percent data). These high specular return data occur mostly at very low wind conditions. The second step to reduce data scatter is through averaging over the 100 km (radius) circle of the altimeter data for each satellite pass over the buoy location. The resulting datasets contain 561 and 1090 data points for the GoA and Hawaii, respectively. Figure 2 shows the scatter plot of σ_0 vs. U_{10} of the two datasets following these preprocessing procedures. The upper bound of the data is determined by the average of the top 10 percent population in each 1 m s^{-1} wind speed bin, shown as stars in the figure. Alternatively, the maximum value in each bin can be used but the result appears to be less representative of the upper bound of $\sigma_0(U_{10})$. Two apparently spurious data points in the GoA dataset (at U_{10} = 17 and 19 m s^{-1}) are excluded in the subsequent analysis. More details on the altimeter/buoy data analysis are given in the subsequent sections.

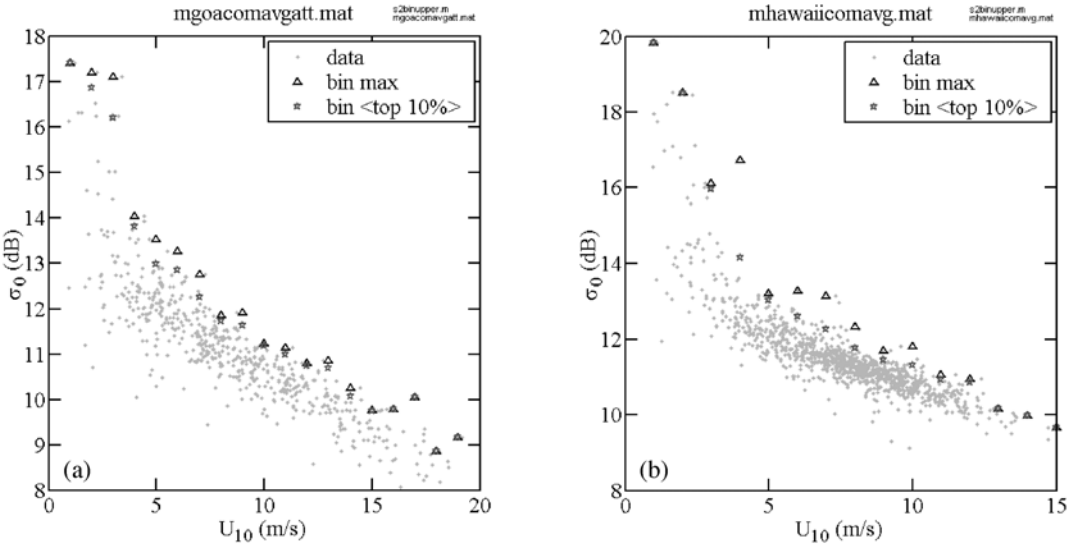

(a) (b)

Fig. 2 — The scatter plot of the altimeter backscattering cross sections and wind speeds. The upper bound of the data is used to derive the wind-induced surface roughness. Empirically, the average of the top 10 percent of the data in each 1 m s^{-1} wind speed bin yields a very good representation of the upper bound of the data. Shown are (a) measurements from the Bering Sea and the Gulf of Alaska, and (b) measurements from the Hawaiian region.

2.5 Breaking Roughness

Figure 3 plots the local wind induced surface roughness measured from the altimeter. The results calculated from both datasets are in excellent agreement. Due to the large altimeter footprint that provides high statistical average, the wind speed trend of the calculated surface roughness is quite "clean" and of excellent quality. For illustration, the CM clean surface data are plotted in the figure for comparison.

The wind-induced roughness is noticeably higher than that expected from the geometric contribution of ocean waves. For comparison, the filtered surface roughness due to wave geometry is calculated from the spectral function assumed to reach equilibrium and saturation condition (Eq. (4)), with the cutoff wavelength set as three times the radar wavelength and plotted as the dashed-and-dotted curve in Fig. 3.

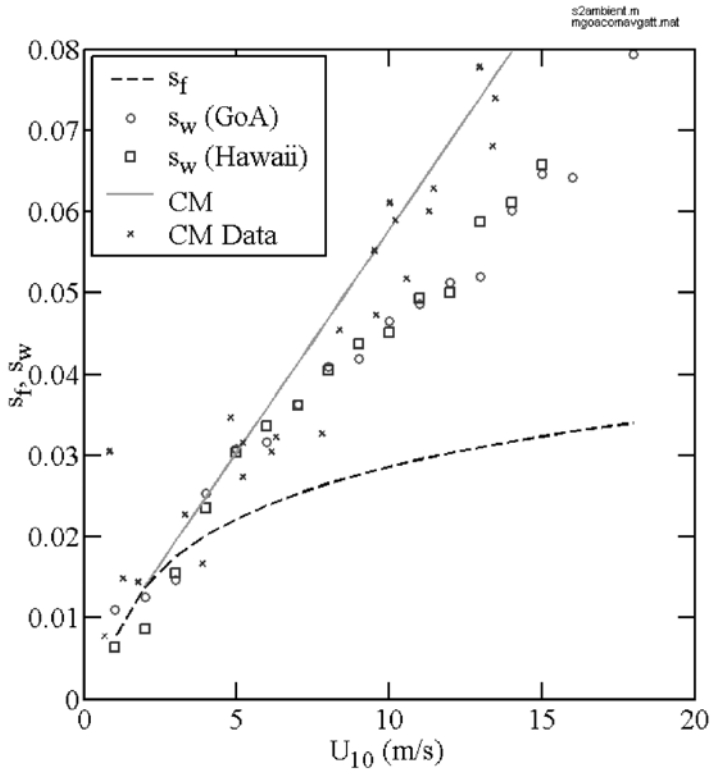

Fig. 3 —The filtered wind-induced surface roughness s_w derived from the TOPEX altimeter and the filtered mean square slopes s_f calculated from the equilibrium and saturation spectrum (Eq. (4)). For comparison, the CM clean surface data are also plotted.

In the low wind condition (U_{10}<3 m s^{-1}), the surface roughness derived from σ_{0u} is slightly less than the filtered mean square slopes calculated from the equilibrium/saturation wave spectral function. Several explanations for the lower-than-expected roughness detected by the altimeter can be offered. For low wind speeds, the wave condition in the altimeter footprint may not reach full equilibrium and saturation. The diameter of the altimeter footprint ranges from a couple of kilometers at low sea state to about 10 km at high sea state (Chelton et al. 1989). In low and variable wind conditions, inhomogeneity of waves with large patches of calm waters may be normal occurrences. Also, slick bands are more likely to form under low wind speeds. Efficient suppression of short surface waves by slicks is a well-known phenomenon and may produce mirrorlike surfaces until wind is sufficiently strong to disrupt the slicks.

The most interesting results shown in Fig. 3 are at medium-to-high wind conditions where altimeter measured roughness becomes higher than the mean square slope contributed by surface waves. The excess of the total filtered wind-induced roughness s_w above the filtered mean square slopes s_f occurs at $U_{10}\approx 3.5$ ms^{-1}. This wind speed is close to the condition of wave breaking inception based on extensive field observations (e.g., Thorpe and Humphries 1980; Wu 1979). Assuming that the wind-induced roughness is mainly contributed by the wave geometry of the local wind sea and the breaking events in the wave field, the data shown in Fig. 3 can be used to provide a quantitative representation of wave breaking in terms of an equivalent roughness (the breaking roughness),

$$s_b = s_w - s_f \,. \tag{10}$$

Wind speed dependence of the breaking roughness follows a power-law relation (Fig. 4) with the exponent of the power-law close to 1.5. The dashed curve that passes through the cluster of data is

$$s_b = 5.6 \times 10^{-4} U_{10}^{1.5}. \tag{11}$$

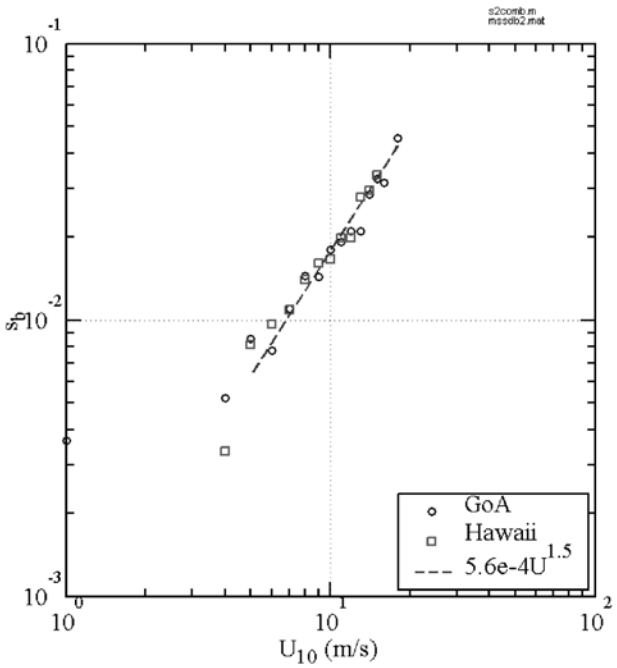

Fig. 4 — The breaking roughness, s_b, calculated from the difference s_w-s_f. The rate of increase of s_b with respect to wind speed follows a power-law function, $s_b = 5.6 \times 10^{-4} U_{10}^{1.5}$ (Eq. 11).

The rapid increase of the breaking roughness at medium and high wind speeds is in contrast to the much slower logarithmic growth of the wave-induced mean square slope. As wind speed increases, the breaking-induced component may becomes the dominant contributor to the total wind-induced roughness. Figure 5 plots the ratio s_b/s_f as a function of wind speed; at $U_{10}>15$ m s^{-1}, $s_b/s_f>1$.

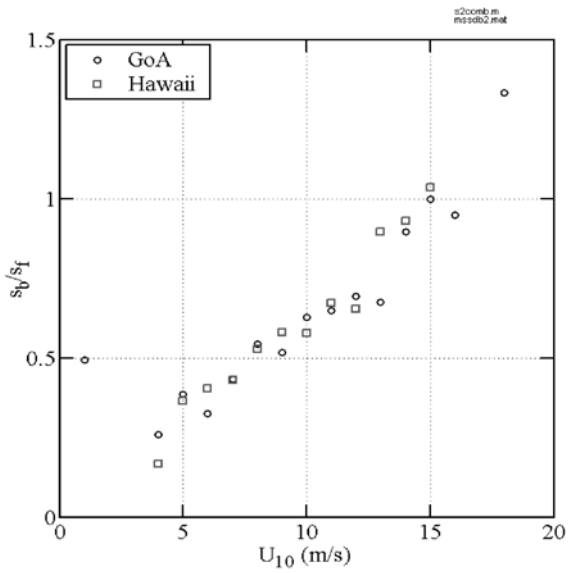

Fig. 5 — The ratio s_b/s_f as a function of wind speed. Breaking roughness becomes an important portion of the ocean surface roughness at medium-to-high wind speeds.

2.6 Discussions

It has been pointed out earlier that the rate of increase of the mean square slope of an equilibrium/saturation spectrum is logarithmic, which is considerably less than the power-law ($U_{10}^{1.5}$) increase of s_b in medium to high wind speeds. The calculations presented above did not consider the CG wave contribution. Recently, in situ measurements of the wavenumber spectra in the CG wave range have been reported (e.g., Hwang et al. 1996; Hara et al. 1994, 1998). Hwang et al. (1996) acquired field data of CG waves with wavelength resolution ranges from 0.004 to 0.06 m. The reported wind speed range is from 0.8 to 5.7 m s^{-1}. The mean square slopes of these CG waves increase linearly with wind speed. Hara et al. (1994, 1998) do not present the mean square slope results but the dimensionless spectral coefficients reported in their experiments are similar to those by Hwang et al. (1996) and the wind speed dependence is also close to linear although the data scatter is considerable.

The filtering operation of the altimeter measurements excludes the difficult problem of CG wave contribution. The wind-induced roughness s_w derived from altimeter is also much larger than the filtered mean square slope of wind-generated waves, s_f. The difference s_w-s_f also increases with wind speed following a power-law function with the exponent of power-law equal to 1.5. Judging from the fact that the slicks maintain their coherent structure in the CM experiment, it is suggested that wave-breaking events, together with short waves, are suppressed by the oil slicks. The slick data of CM therefore represent a reliable measurement of wind-induced roughness minus the wave-breaking contribution. The altimeter filtering process as well as the optical measurement in clean water does not alter the sea surface condition and the measured wind-induced roughness includes both mean square slope and breaking contributions of wind waves.

2.7 Conclusions

Remote sensing has become an important tool for ocean research. Ocean surface roughness is a key parameter for the interpretation of remote sensing data. Performing in situ measurements of the ocean surface roughness remains a very difficult task. In comparison, acquiring the radar scattering cross section from the ocean surface is relatively easy. Over the last several decades, countless datasets have been

collected from satellites, aircraft, ships and ocean towers. These datasets represent a tremendous wealth that can be used to improve our understanding of the ocean surface roughness.

In this section, the backscattering cross sections measured by the TOPEX Ku-band altimeter and collocated wind measurements from NDBC buoys over a 7-year period are analyzed to extract the wind-induced ocean surface roughness. The range of wind speeds and sea state conditions from spaceborne measurements exceeds the range of the existing in situ datasets. The analysis procedure of the altimeter data eliminates the issue of ambient roughness attenuation of altimeter cross sections to be further studied in Section 3 by using the upper bound of $\sigma_0(U_{10})$ for retrieving the wind-induced ocean surface roughness s_w. Also, the altimeter filtering operation excludes the contribution of CG waves and simplifies the data analysis and interpretation.

Comparing with the filtered mean square slope of a local wind sea s_f, it is found that s_w exceeds s_f at $U_{10}\approx3.5$ ms^{-1}. The characteristics of the roughness excess of altimeter are similar to those of the roughness difference between the clean and slick conditions derived from the sun glitter data of Cox and Munk (1954). A hypothesis is put forth that the difference $s_b = s_w - s_f$ is due to wave breaking; that is, s_b is an equivalent roughness of wave-breaking events. The breaking roughness increases with wind speed following a power-law function, $s_b = 5.6 \times 10^{-4} U_{10}^{1.5}$. At medium-to-high wind speeds, the breaking roughness becomes as important as the mean square slope of the wind wave geometry (Fig. 5). The results from this analysis strongly suggest that calculation of the ocean surface roughness based on the mean square slope integrated from the surface wave spectrum may produce serious underestimation of the total wind-induced ocean surface roughness.

3. AMBIENT ROUGHNESS DERIVED FROM ALTIMETER RETURNS

3.1 Background

Radar sea returns are related to wind speeds through the ocean surface roughness, mainly attributed to wind-generated surface waves in the ocean. Using satellite altimeter output, sea surface wind speed can be obtained every 7 km along a groundtrack. Comparisons with in situ buoy measurements show that the accuracy of altimeter wind measurements is approximately 1.8 m/s over the global scale, and close to 1.2 m/s in a low sea state region (e.g., Brown 1978, 1981, 1990; Brown et al. 1981; Chelton and Wentz 1986; Dobson et al. 1987; Witter and Chelton 1991; Wu 1992; Ebuchi and Kawamura 1994; Freilich and Challenor 1994; Gower 1996; Hwang et al. 1998). The measured radar intensity (the normalized radar cross section), σ_0, however, is found to differ significantly from theoretical calculations (e.g., Brown 1990). Up to this date, the operational wind speed algorithms are based on empirical or statistical correlation derived from collocated and simultaneous measurements from in situ buoys and spaceborne altimeters.

Hwang et al. (1998) investigate the attenuation of the radar cross section due to waves much longer than the radar wavelength. Their analysis produces a solution that indicates the potential accuracy of altimeter wind speed retrieval is much better than the figures currently accepted. The root mean square (rms) wind speed difference between buoy and altimeter data can be reduced by more than 40 percent. Further analysis presented in this section indicates that the improvement of calculated and measured altimeter cross section is due to the incorporation of ambient roughness in the analysis presented in Hwang et al. (1998). Two primary contributors of the ambient component are (a) fluctuations due to turbulence processes not related to local wind conditions and (b) swell that originated in distant regions.

The influence of the significant wave height on the altimeter return at a given wind speed has been noted since the late 1980s. Earlier efforts to incorporate wave height parameters into the altimeter wind speed algorithms include multiple regressions (Monaldo and Dobson 1989; Lefevre et al. 1994) and introducing a wave age dependence on the altimeter return (Glazman and Greysukh 1993). The former approach uses the altimeter output and reference datasets (e.g., collocated buoy measurements or wind speeds from other satellite sensors) to establish a bivariable dependence of wind speed on the altimeter

cross section and significant wave height. The later eventually derives a pseudo-wave age using the altimeter outputs of wind speed and significant wave height. There appear to be improvements in these two-parameter algorithms but the comparisons with in situ data are not conclusive. A more extensive discussion of these efforts is given by Lefevre et al. (1994).

In this section, collocated and simultaneous altimeter and buoy data in the GoA dataset are compiled to establish the functional relationship of the ambient roughness. Analytical calculation of the cross-section incorporating the ambient roughness function is found to be in excellent agreement with measurements, as compared to the standard wind speed algorithms (Brown et al. 1981; Witter and Chelton 1991). The ambient roughness function is further applied to other datasets in the Gulf of Mexico and Hawaii regions and also result in excellent performance.

As described in Section 3.2, the ranges of wind speeds and wave heights in the GoA datasets are much wider than those of the Gulf of Mexico dataset described by Hwang et al. (1998). The altimeter return is noticeably reduced with increasing wave heights for a given wind speed. Such sea state influence is consistent with the results reported by Anderson et al. (1999) and Gourrion et al. (2000). Section 3.3 presents an analysis of the functional relation between altimeter signal attenuation and ambient roughness. Using the GoA dataset, the sea state influence on the ambient roughness S is investigated. An empirical function of $S(U_{10}, H_s)$ is presented in Section 3.4, where U_{10} is the neutral wind speed at 10 m elevation and H_s is the significant wave height. Additional discussions on the dependence of sea surface roughness on wind speed, ambient roughness attenuation, and several other issues related to wind speed algorithms are presented in Section 3.5. Finally, Section 3.6 presents the summary and conclusions.

3.2 Bering Sea and Gulf of Alaska Dataset

NDBC buoys 46003 and 46035 are located near TOPEX groundtrack crossovers. Buoy and altimeter data within 100 km and 0.5 h time lag are merged to form four data files. The duration of coverage is from 1992 to 1999. Some fundamental statistics of sea state conditions of the data files are shown in Table 2. Additional descriptions of buoy and TOPEX data processing can be found in Hwang et al. (1998). These four data files are combined to form the GoA dataset.

Table 2 — Basic Statistics of the Sea State Conditions of the Data Files Collected in the Gulf of Alaska and the Bering Sea

	Max U_{10}	Min U_{10}	Max H_s	Min H_s	No. of raw data points
	(m/s)	(m/s)	(m)	(m)	
T028B635	20.2	0.1	7.6	0.0	4738
T101B630	18.3	0.9	6.2	0.4	4559
T091B603	17.9	0.0	8.0	0.9	4089
T100B603	18.1	0.3	7.9	1.0	3922

As noted earlier, some of the large data scattering cross sections are due to the deficiency in the altimeter waveform algorithm in treating specular returns from very calm surfaces. These specular data are out of the application range of the MCW algorithm. The SB algorithm does not respond well to those specular data either. The specular data are excluded (see Section 2.4). These measurements described in Table 2 are combined and the scatter plot of altimeter cross-sections and wind speeds is shown in Fig. 6(a). To illustrate the sea state influence, the measurements are sorted according to the significant wave height. The data scatter is considerable, especially at lower wind speeds. Despite the large data scatter, stratification of $\sigma_0(U_{10})$ with H_s is distinguishable. To reduce clutter, for each buoy datum (i.e., per satellite pass) the TOPEX measurements within the 100-km (radius) circle are averaged. The number of data points averaged ranges between 28 and 33 for each buoy measurement. The results are shown in Fig.

6(b). A trend of decreasing σ_0 with increasing H_s for the same U_{10} is suggested. The average dataset contains 565 data points (Fig. 7). The wind speed histogram and the wind speed function of σ_0 variations in the final dataset are similar to those of the raw dataset, suggesting that the statistical properties of the raw data are not altered by the averaging procedure. The histogram of wind speeds is approximately Rayleigh distribution, shown as connected pluses in Fig. 7(b). The variability of σ_0 as a function of wind speed (represented by the standard derivation of σ_0 in each wind speed bin) is shown by connected circles in Fig. 7(b). Of special interest is the noticeable enhanced σ_0 variability at mild-to-moderate wind speed range (U_{10}< ~8 m/s). As shown in Section 3.3, this is a characteristic feature of the ambient attenuation.

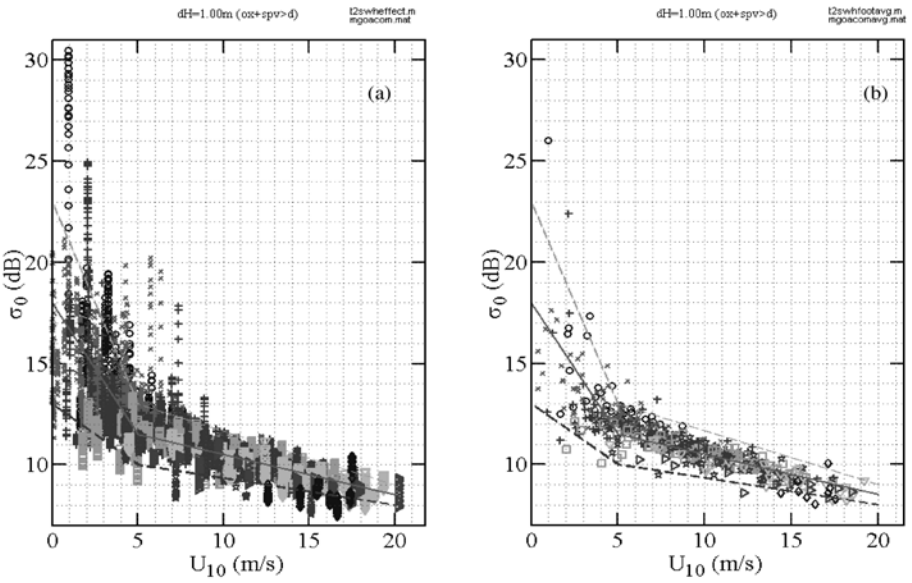

(a) (b)

Fig. 6 — The scatter plot of altimeter cross-sections and wind speeds. The data are divided into subsets of different wave heights and plotted with different symbols (o: $0<H_s\le1$, ×: $1<H_s\le2$, +: $2<H_s\le3$, □: $3<H_s\le4$, ★: $4<H_s\le5$, ∇: $5<H_s\le6$, ▷: $6<H_s\le7$, ◇: $7<H_s\le8$ m). (a) All data within 100 km between buoy and altimeter measurements, the maximal time lag is 0.5 h. (b) Same as (a) but for each buoy measurement, the altimeter data within 100 km are averaged.

In Fig. 8, data in different H_s bins are plotted in individual panels. The whole dataset is plotted in the panel marked (all). The remaining eight panels, marked (1) through (8), are the subsets in 1-m H_s bins [i.e., (1): $0<H_s\le1$, (2): $1<H_s\le2$, …, (8): $7<H_s\le8$ m]. The gradual decreasing of σ_0 with increasing H_s for the same U_{10} range is discernable. For example, from panels (1) to (7), there are numerous data points in the common wind speed range of $5\le U_{10}\le10$ m/s. The groups of data in this range show a continuous trend of decreasing σ_0 with increasing H_s. Three identical curves forming approximately the upper, middle, and lower bounds of the full dataset are superposed on each panel to serve as visual aid in the comparison. A reduction of 1.5 to 3 dB in σ_0 is seen in this wind speed range when H_s increases from 1 to 7 m. The degree of σ_0 attenuation is less severe at higher wind speeds. Very similar stratifications of $\sigma_0(U_{10})$ with H_s are described by Anderson et al. (1999) and Gourrion et al. (2000). In the former, collocated and simultaneous measurements of TOPEX altimeter and buoy datasets are used for analysis. In the latter, collocated and simultaneous measurements of TOPEX and NSCAT are used. The data population using multiple satellites is more than 90,000, a number that is difficult to match by in situ sensors.

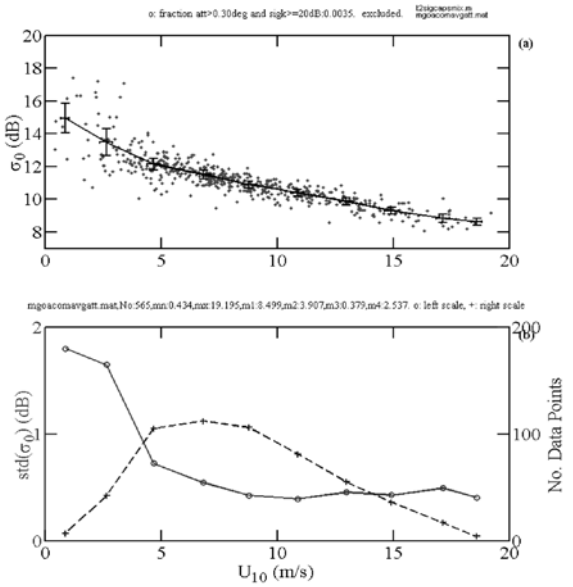

Fig. 7 — The Bering Sea and Gulf of Alaska data files. (a) The scatter plot of the combined dataset (dots) and the mean (pluses) and standard deviation (error bars) of bin-average results (2.25 m/s bin size). (b) The histogram of bin-average wind speeds (pluses, right scale) and the standard deviation of σ_0 in each wind speed bin (circles, left scale).

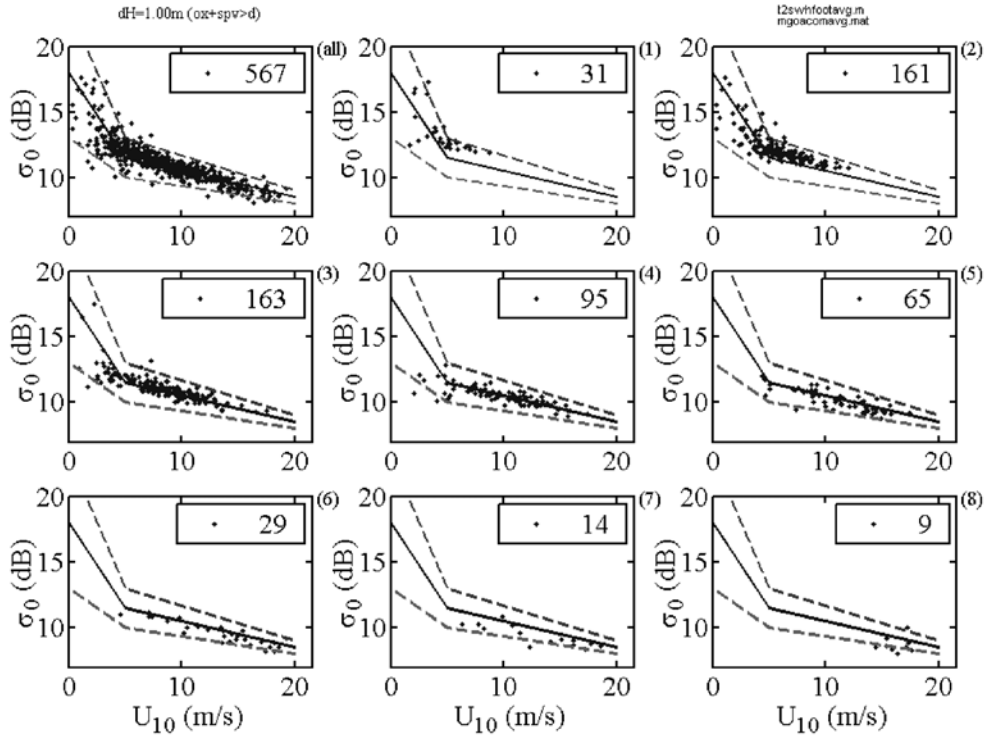

Fig. 8 — The scatter plot of altimeter cross sections and wind speeds. The data are divided into subsets of different wave heights and plotted in individual panels for clarity. The panels are labeled (1), (2), … (8) for wave height bins of [0-1], [1-2], …, [7-8] m. The panel labeled (all) is all data combined. The number of data points in each subset is indicated in the legend of each panel. For visual aid, three curves forming approximately the upper, middle, and lower bounds of the full dataset are superposed on each panel.

3.3 Altimeter Cross Sections and Surface Roughness

Wind speed is derived from the altimeter backscattering cross section σ_0 through the link of the ocean surface roughness. To the first order, the relation between σ_0 and surface roughness is (e.g., Barrick 1968; Brown 1978)

$$\sigma_0 = \frac{R_0}{s_{ft}}, \tag{12}$$

where R_0 is the Fresnel reflection coefficient for normal incidence, and s_{ft} is the total filtered surface roughness contributing to altimeter backscatter. Hwang et al. (1998) separate the filtered roughness into short and long scales and derive a slightly different formula,

$$\sigma_0 = \frac{R_0}{s_f}\sqrt{\frac{s_f}{s_f + 2v_t}}, \tag{13}$$

where s_f is the filtered mean square slope of short-scale waves, and v_t is the mean square slope of long-scale waves, including a local wind-generated component s_t and an ambient component S contributed by processes not related to local wind. That is,

$$v_t = s_t + S. \tag{14}$$

For $S = 0$, $s_{ft} = s_f + s_t$.

The square root solution to Eq. (13) is a consequence of using a one-dimensional (1-D) Gaussian distribution function in the derivation. If a two-dimensional (2-D) Gaussian distribution is applied, the solution is

$$\sigma_0 = \frac{R_0}{s_f + v_t}, \tag{15}$$

which is identical to Eq. (12) as $s_{ft} = s_f + s_t$ by definition if the ambient roughness is not considered (i.e., $S = 0$). It becomes clear that the ambient parameter simply contributes more roughness on the surface for radar scattering. Thus an understanding of the ambient roughness term is a key factor for improving the accuracy of altimeter wind retrieval.

As shown in Section 3.4, computationally Eqs. (13) and (15) produce very similar results. For very low wind speeds, the 1D solution (referred to as H1D hereafter) appears to more closely follow the data trend of the measurements than does the 2D solution (referred to as H2D hereafter). It is possible that at low wind conditions, the ambient components are composed of linear undulations that fit the 1D description better than the 2D. Therefore, the results from both 1D and 2D are presented in the following. From Eqs. (13) and (15), S can be expressed as

$$S_{1D} = \frac{1}{2}\left[\left(\frac{R_0}{\sigma_0}\right)^2 \frac{1}{s_f} - s_f - 2s_t\right], \tag{16}$$

and

$$S_{2D} = \frac{R_0}{\sigma_0} - s_f - s_t, \tag{17}$$

where subscript 1D represents results using the 1D Gaussian solution, and subscript 2D for the 2D Gaussian solution. Applying Eqs. (16) and (17), the properties of S can be studied in detail using simultaneous and collocated measurements of σ_0 from altimeter and U_{10} and H_s from buoys.

The altimeter signal attenuation, $\Delta\sigma$, due to ambient roughness (referred to as the ambient attenuation hereafter) can be quantified by dividing Eqs. (13) and (15) by the reference solutions of the corresponding equations with $S = 0$, which leads to the following equations,

$$\Delta\sigma_{1D} = \left(\frac{s_f + 2s_t}{s_f + 2(s_t + S)} \right)^{1/2}, \tag{18}$$

and

$$\Delta\sigma_{2D} = \frac{s_f + s_t}{s_f + s_t + S} = \frac{s_{ft}}{s_{ft} + S}. \tag{19}$$

Figure 9(a) illustrates the analytical solution of $\Delta\sigma$ as a function of wind speed for different levels of the ambient roughness, with S varying from 0 to 0.015. An important feature of the ambient attenuation is that for a given level of ambient roughness, $\Delta\sigma$ as a function of U_{10} is relatively flat in the high wind speed region, say, U_{10}>10 m/s, and the excursion of $\Delta\sigma$ becomes increasingly larger toward lower wind speeds. This is an interesting result because it is frequently found that in a given dataset of the observed altimeter cross sections, the level of signal variability is typically much higher at the lower wind speed range than that at the higher wind speed range. This is a counterintuitive result because as wind speed increases, more complex processes such as wave breaking, turbulence, whitecaps, and foam enter the scattering process. As a consequence, one expects that the data scatter of altimeter cross sections grows larger as the wind speed increases. However, typical results of the σ_0 variability as a function of wind speed display a reverse trend.

The puzzling result that less data scatter occurs in more complicated high wind environment can be explained by the fact that the ambient roughness constitutes a much smaller fraction of the ocean surface roughness at the high wind condition. The trend of increasing σ_0 variability toward low wind speed (Fig. 9(a)) is in fact a reflection of the relative weighting of the ambient roughness and the filtered roughness. Figure 9(b) shows the observed wind speed dependence of the σ_0 variability, which is represented by the standard deviation of σ_0 within a wind speed bin. The data shown are from the Gulf of Mexico dataset (Hwang et al. 1998) and the GoA dataset (Section 3.2). The ensemble average of the calculated ambient attenuation shown in Fig. 8(a) can be interpreted as the expected signal variability due to unknown background ambient roughness (with a uniform distribution of S between 0 and 0.015). The ensemble averages for H1D and H2D are superimposed with the data in Fig. 8(b). The similarity between the measured cross-section variability and the computed ambient attenuation is evident.

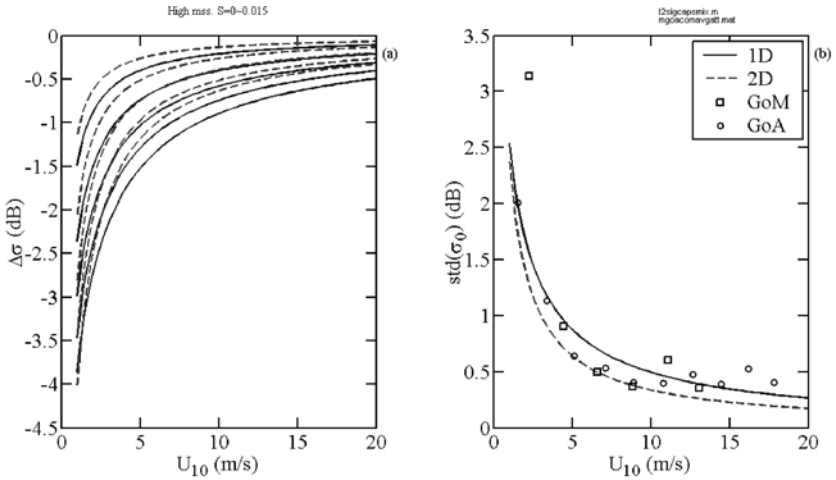

Fig. 9 — (a) Calculated attenuation of the altimeter cross section $\Delta\sigma$ due to ambient roughness S. The level of S varies from 0 to 0.015, increasing downward in the figure. The solid curves are based on the assumption that the pdf (probability distribution function) of ambient waves is 1-D Gaussian and the dashed curves is 2-D Gaussian. (b) The magnitude of the ensemble average of (a) compared to the observed variability of altimeter cross sections as a function of wind speed. □: Gulf of Mexico dataset (Hwang et al. 1998), o: Bering Sea and Gulf of Alaska dataset (Section 2).

3.4 Ambient Roughness and Sea State Influence

Applying Eqs. (16) and (17), the ambient parameter based on 1D and 2D solutions can be calculated from altimeter σ_0, and s_f and s_t calculated from buoy U_{10}. Obviously, the quantitative outcome of S depends on the wind speed functions of s_f and s_t.

Over the last half century, there are only a handful of field measurements reporting mean square slopes and wind wave conditions (e.g., see review by Hwang 1997). These field data invariably show a linear correlation between mean square slopes and wind speeds, although from the saturation spectral calculation, the mean square slope of long waves increases logarithmically with wind speed (e.g., Phillips 1966; Wu 1972; Hwang and Wang 2001). The issue on the wind speed functions for s_f and s_t is further complicated by uncertainties in choosing the proper wavelength range to calculate the filtered roughness from the wavenumber spectrum. For example, Jackson et al. (1992) list the proposed separation length scales cited in several published papers. The range of the numerical values varies from 1.5 to 40. This large range of the separation length scales reflects directly the uncertain state of knowledge on the directional wavenumber spectral models now in use. Further discussion of this issue is deferred to Section 3.5.

We feel that it is too speculative at this stage to pursue refinement of the wind speed function of the filtered roughness component. The choice of a linear wind speed dependence of s_f and s_t is based on two considerations. The first one is the empirical evidence of field measurements as discussed by Hwang (1997) and briefly summarized in the last paragraph. The second consideration is a practical one, which is to eventually produce an inversion function for wind speed retrieval from altimeter outputs of cross section and significant wave height, that is, $U_{10}(\sigma_0, H_s)$, for operational applications. In this respect, the derived ambient roughness S presented in the latter part of this section contains wind-induced roughness contributions due to our insufficient understanding of the wind speed function and the wavenumber spectrum of the surface roughness.

The constants in the linear functions relating wind speeds and filtered mean square slopes can be determined through fitting the analytical computation (by Eq. (13) or (15) with $S = 0$) to the upper bound of the measured altimeter cross sections. Fitting to the upper bound is done since the ambient roughness not associated with local wind introduces additional attenuation, therefore, the measured cross section should be below the curve of analytical computation considering wind-induced roughness only. The procedure yields the following filtered surface roughness functions (Fig. 10)

$$s_f = 3.62 \times 10^{-3} U_{10}, \tag{20}$$

and

$$s_t = 4.0 \times 10^{-4} U_{10}. \tag{21}$$

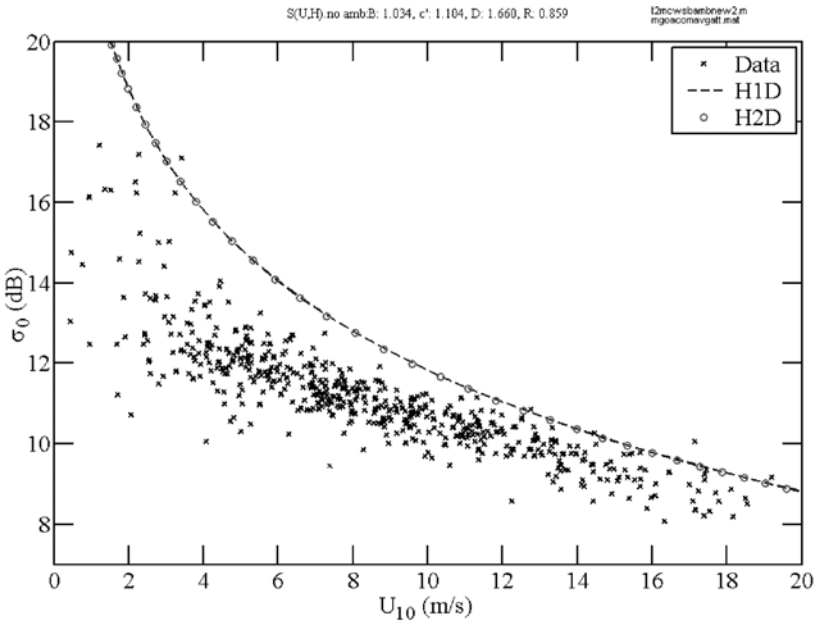

Fig. 10 — Comparison of measured and calculated cross section without consideration of the ambient roughness. The filtered mean square slope function (Eqs. (9-10)) is obtained from matching the upper bound of the measured cross section data.

Examples of the calculated S_{1D} and S_{2D} using Eqs. (16-17) and Eqs. (20-21) are shown in Fig. 11. The general trend of decreasing S with increasing U_{10} is universal for most H_s bins. To illustrate this feature, the data in nine H_s bins (1-m bin size) are plotted separately in the upper panels of the figure. The upper left nine panels are for H1D, and the upper right nine panels for H2D. Similarly, the general trend of increasing S with increasing H_s is found in most U_{10} bins (2.25-m/s bin size). The dependence of S on H_s is shown in the lower panels with the lower left nine panels for H1D, and the lower right nine panels for H2D.

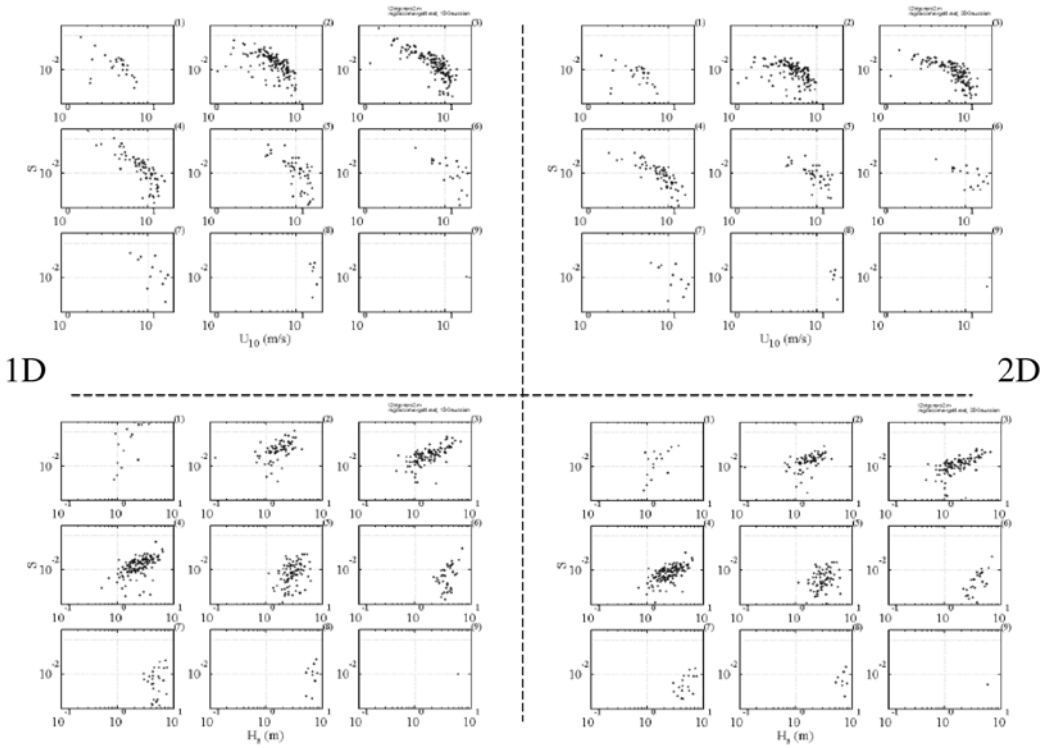

Fig. 11 — The calculated ambient roughness as a function of wind speed and wave height. The data in each H_s and U_{10} bin (1-m and 2.25-m/s bin sizes) are plotted in a separate panel for clear identification of the trend. The left panels are based on the 1-D Gaussian assumption. The right panels are based on the 2-D Gaussian assumption. The top panels are $S(U_{10})$ for H_s bins. The bottom panels are $S(H_s)$ for U_{10} bins.

Numerical experiment is carried out to obtain the function $S(U_{10}, H_s)$. The goal is to minimize bias and rms difference, maximize correlation coefficient, and approach unity of the regression coefficient. The experiment yields the following functional form for $S(U_{10}, H_s)$,

$$S = S_0 f_1(U_{10}) f_2(H_s, U_{10}) + f_3(H_s) + S_{00}, \tag{22}$$

in which

$$f_1(U_{10}) = \left\{1 - \left(\frac{U_{10}}{B_U}\right)^{\alpha_1}\right\}^{\beta_1}, \tag{23}$$

$$f_2(H_s, U_{10}) = B_{HU} H_s^{\alpha_2 \left[1 - \left(\frac{U_{10}}{B_U}\right)^{\alpha_1}\right]}, \tag{24}$$

and

$$f_3(H_s) = B_H H_s^{\alpha_3}. \tag{25}$$

The parameters used in Eqs. (22 through 25) are listed in Table 3.

Table 3 — Parameters used in the Ambient Roughness Functions $S(U_{10},H_s)$ (Eqs. (22-25))

	S_0	α_1	α_2	α_3	β_1	B_U	B_{HU}	B_H	S_{00}
H1D	0.02	0.3	0.5	0.5	1.08	20	2.75	0.0008	0.0075
H2D	0.012	0.4	1.15	0.1	1.2	20	1.3	0.005	0.0035

The statistics of comparison between calculated and measured cross sections are listed in Table 4, showing general improvements over the other algorithms when the ambient attenuation is considered. For the GoA dataset (Table 4(a)), using the MCW results as a reference, the rms difference is reduced to between 0.62 and 0.66 dB (0.75 dB for MCW); the data bias is mostly less than 0.03 dB (0.15 dB for MCW); the regression coefficient approaches unity, the values are 0.998 to 1.000 (1.012 for MCW); and the correlation coefficient also increases to between 0.88 to 0.90 (0.85 for MCW). Figure 12 shows the scatter plots of calculated and measured σ_0.

Verification of the applicability of the ambient roughness function (Eqs. (22-25)) for general application is carried out with other independent datasets collected in the Gulf and Mexico and near the Hawaii region. The former dataset has 498 and the latter has 1032 data points, as compared to 565 in the GoA dataset. Using the MCW results as the yardstick for comparison, the calculations based on the analytical solutions (Eqs. (13 and 15) with Eqs. (22-25) for the ambient roughness) show excellent performance (Table 4(b) and 4(c)).

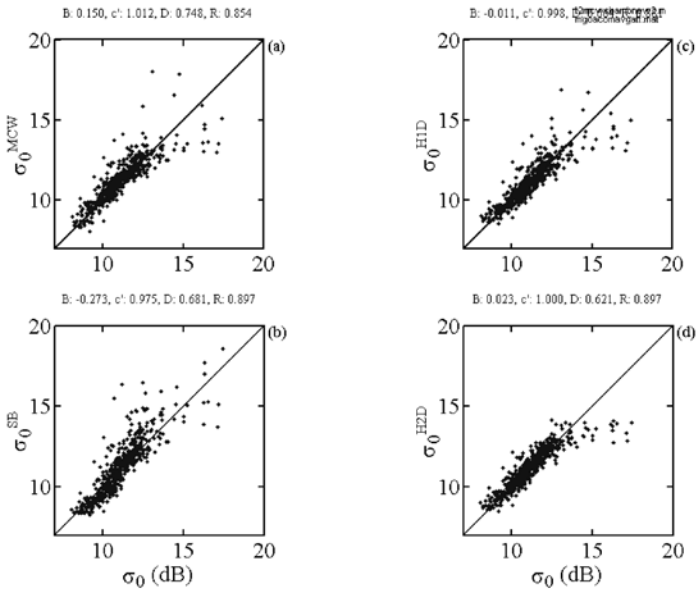

Fig. 12 — A comparison of calculated and measured σ_0 using different algorithms: (a) MCW, (b) SB, (c) H1D, and (d) H2D

Table 4 — Statistics of Comparison Between Measured and Calculated Altimeter Cross Sections

	Bias (dB)	Regression Coefficient	RMS Difference (dB)	Correlation Coefficient
(a) GoA	**(565 points)**			
MCW	0.150	1.012	0.748	0.854
SB	-0.273	0.975	0.681	0.897
H1D	-0.011	0.998	0.664	0.881
H2D	0.023	1.000	0.621	0.897
(b) GoM	**(498 points)**			
MCW	-0.250	0.975	0.969	0.807
SB	-0.270	0.976	0.909	0.826
H1D	-0.257	0.976	0.911	0.823
H2D	-0.054	0.992	0.874	0.824
(c) Hawaii	**(1032 points)**			
MCW	0.042	1.003	0.371	0.872
SB	-0.373	0.968	0.547	0.872
H1D	-0.178	0.984	0.412	0.879
H2D	-0.078	0.993	0.384	0.869

3.5 Discussions

3.5.1 Ocean Surface Roughness

To the first order of approximation, the relation between the altimeter cross section and the wind-induced surface roughness is expressed as Eq. (12). This formula overestimates the wind-induced ocean surface roughness, especially in the mild-to-moderate wind speed range (e.g., see Fig. 4 by Hwang 1997 and the associated discussions). This is a perplexing result because many of the complex nonlinear processes in the surface wave field and the interaction of radar and surface waves are less severe in the mild-to-moderate wind speeds. The agreement between theoretical calculations and empirical measurements (of mean square slopes, radar cross sections, or wind speeds) should be in better agreement in such situations.

A different way of looking at this issue is to investigate the calculated and measured altimeter cross sections for a given mean square slope function. There are several sets of ocean measurements correlating mean square slopes with wind and wave conditions (Cox and Munk 1954, 1956; Hughes et al. 1977; Tang and Shemdin 1983; Hwang and Shemdin 1988; Hwang et al. 1996). A detailed review is presented by Hwang (1997). All these optical measurements conform to the linear wind speed dependence as originally suggested by Cox and Munk (1954). After correction of several data points that are obviously influenced by large swell not associated with local wind conditions, the combined field data fit the following equation

$$s_{total} = 5.12 \times 10^{-3} U_{10} + 1.25 \times 10^{-3}, \tag{26}$$

with data scattering within a factor-of-two envelope (Hwang 1997). The optically measured mean square slope represents a conservative upper limit of the filtered mean square slope of the Ku-band altimeter on TOPEX. Figure 13(a) shows the calculated and measured σ_0 based on Eqs. (12) and (26). Even with such a high mean square slope function, the calculated curve is still above the measured cross sections in the mild-to-moderate wind speed range (U_{10}<~7 m/s). This indicates that the apparent roughness perceived by the altimeter is much higher than the optical limit of the ocean surface slope. This is an illogical result that has been discussed by Hwang (1997) and Hwang et al. (1998).

If a more realistic level of the filtered roughness is specified, the computational curve will move further upward from the one based on the total optical mean square slope. An accurate prescription of the filtered slopes requires the knowledge of the wavenumber spectrum and a precise formula to determine the length scale separating the diffraction and reflection roughness components. Our understanding of these two pieces of information in the short scale waves needed for Ku-band calculation is not very good. For example, Jackson et al. (1992) list the separation length scales cited in several papers, the numerical values range from 1.5 to 40. The state of knowledge on the directional wavenumber spectrum in the short wave range is equally vague. Instead of speculating on these issues, we take the approach of estimating the filtered roughness from the altimeter data. As discussed in the previous sections, processes not associated with local wind conditions introduce ambient roughness into the altimeter scattering from the ocean surface. Therefore, the calculated results considering only wind-induced roughness should yield the upper bound of measured scattering cross sections. Figure 10 is reproduced as Fig. 13(b) here for comparison. Using the upper bound of the measured σ_0 as a guideline, the wind speed function of the filtered mean square slopes can be represented by Eqs. (20) and (21).

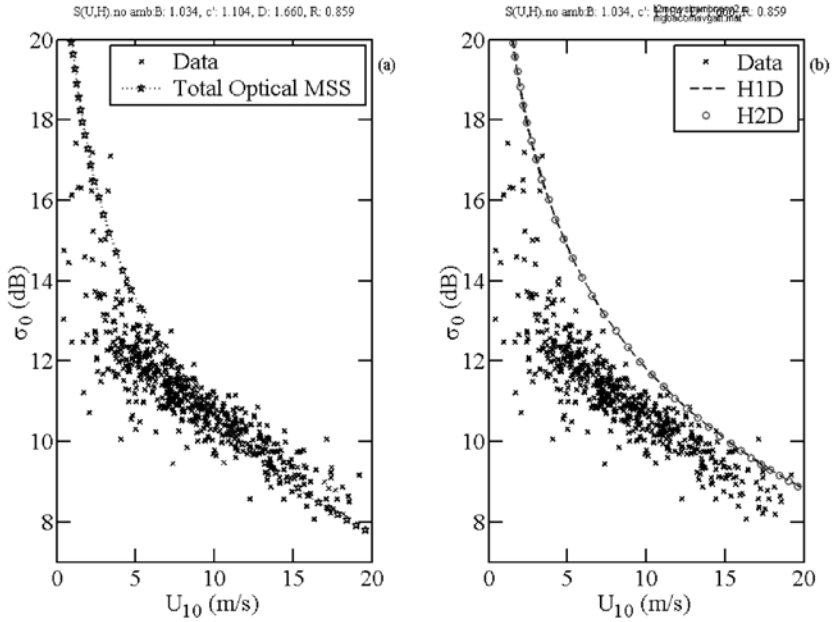

Fig. 13 — (a) A comparison of measured and calculated $\sigma_0(U_{10})$ using the total mean square slope derived by optical sensors (Eq. (26)). (b) Calculations based on the roughness function (Eqs. (20-21)) that yields a good representation of the upper bound of measured cross sections.

3.5.2 Ambient Attenuation

The ambient attenuation, $\Delta\sigma$, can be calculated from the difference between the measured and calculated cross sections using Eq. (13) or (15) with S = 0. The results are plotted in Fig. 14 in light

background and with error bars representing the mean and standard deviation of the bin-average wind speed.

These measured attenuations are compared with the analytical solutions (Eqs. (18-19)). The ambient roughness in Eqs. (18) and (19) is calculated by Eqs. (22 through 25). For clarity of presentation, the continuous curves shown in Fig. 14 is based on a constant significant wave height, $H_s = 1$ m. (Calculations using actual wave heights are not a monotonic function of wind speed and appear as clusters in the figure. All statistics described in the text, however, are based on computations using actual wave heights.) The agreement in the wind speed trends between the measured and computed ambient attenuations is excellent.

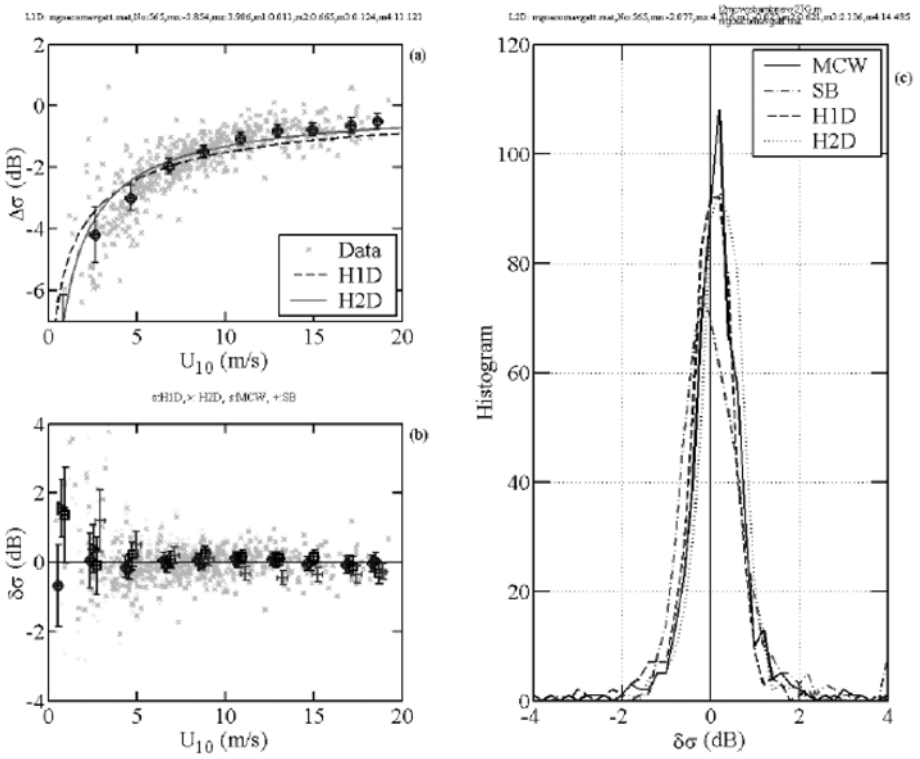

Fig. 14 – (a) A comparison of the measured and calculated ambient attenuation (dashed line: H1D, Eq. (18); solid line: H2D, Eq. (19)). The measured data ares shown as light crosses in the background, the wind speed bin average are shown in circles, with error bars of one standard deviation of the data in the wind speed bins. (b) The net difference of measured and computed cross sections $\delta\sigma$ using difference algorithms. The scatter plots are shown in light color on the background, and bin averages by symbols with error bars. o: H1D, Δ: H2D, □: MCW, and +: SB. (c) The histograms of $\delta\sigma$ computed by different algorithms (see legend).

An example of the net difference ($\delta\sigma$) between the measured and calculated cross sections taking into account the ambient roughness is displayed in Fig. 14(b). The scatter plots of the data based on 1D (circles) and 2D (triangles) solutions are all mixed together and difficult to distinguish. They are displayed in light color on the background. The mean value and standard deviation of each solution are shown as error bars (staggered in the horizontal direction to separate different algorithms). The results of MCW (squares) and SB (pluses) are also shown for reference. The cross section difference of the SB algorithm has a distinctive wind speed trend. The calculated results from the analytical solutions that take into account the ambient attenuation show only minor wind speed trend (compare Fig. 14(b) with Fig. 14(a)). Over a broad range of wind speeds, the cross-section difference is much less than 1 dB. The overall performance of the analytical solutions is comparable to the MCW calculation. Histograms of the

cross-section differences based on different algorithms are shown in Fig. 14(c). For a perfect algorithm, the distribution function of $\delta\sigma$ approaches a delta function centered at zero. The moments of the distribution function represent a measure of the quality of the algorithm. The first two moments of the distribution are the bias and rms difference shown in Table 4.

The calculated results of $\sigma_0(U_{10})$ incorporating ambient roughness are shown in Fig. 15. For clarity, the continuous curves shown in Fig. 15(a) are calculated with H_s = 1 m. Calculations with actual wave heights are shown in Fig. 15(b). These computed results pass through the center of the measured data cluster and match the data trend very well. At the low wind speed range, the 1D solution appears to be in better agreement with measurements (and MCW) than is the 2D solution. For comparison, the MCW and SB results are also shown.

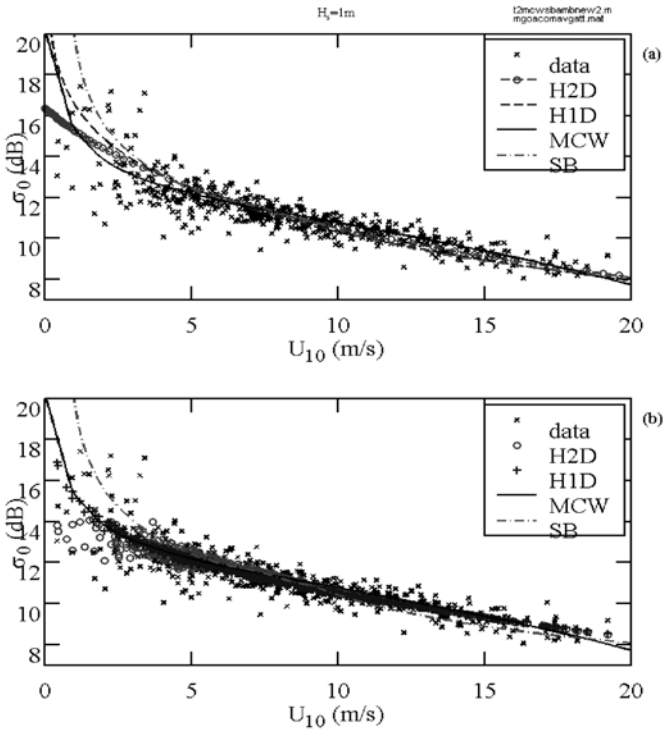

Fig. 15 — Comparison of the measured and calculated $\sigma_0(U_{10})$ with ambient roughness (Eqs. (22-25)) incorporated in the computation. The analytical solutions shown in (a) are calculated with H_s=1 m, and in (b) with actual wave heights.

3.5.3 Alternative Explanations of Discrepancies Between Calculations and Measurements

Several interpretations have been offered to explain the discrepancies between measured and computed cross sections. The more frequently cited explanations are discussed below.

3.5.3.1 Effective Fresnel Reflection Coefficient

Typically the value of R_0 is reduced from the analytical value of 0.61 (e.g. Klein and Swift 1977) to about 0.36 (e.g., Valenzuela 1978; Jackson et al. 1992). This change shifts the calculated curves in Fig. 13 about 2.1 dB downward and does not improve the difference between the wind speed trends of the computed and measured cross sections.

The justification for introducing a reduced effective reflection coefficient is usually attributed to wave breaking, which produces whitecaps and foamy surface that reduce the radar reflection (e.g., Zheng et al. 1983). If this is the case, the effective R_0 decreases toward higher wind speeds. If the wind speed dependence on the Fresnel reflection coefficient is applied, the agreement between the wind speed trends of the calculated and measured cross sections deteriorates further from that using a constant R_0 (Fig. 13).

3.5.3.2 Diffraction Effect Due to Waves Much Shorter than the Radar Wavelength

By carrying out the analytical solution of the scattering problem to a higher order, diffraction due to surface waves shorter than the radar wavelength results in an attenuation of the backscattered signal. The diffraction effect is proportional to the spectral density of short waves. Because short waves increase with wind speed, the diffraction attenuation also increases with wind speed (Fig. 13 of Jackson et al. 1992). Similar to the modification of the reflection coefficient, the diffraction attenuation increases toward higher wind speeds. Applying this correction, the calculated curves in Fig. 13 of this report tip downward in the high wind region, and the discrepancy between computed and measured cross sections worsens.

3.5.3.3 Probability Distribution Function (Pdf) of Surface Slopes

Brown (1979) investigates the distribution function of sea surface slopes for low sea state conditions using the GEOSAT waveform plateau and attitude/specular gate outputs. The result indicates that if a Gaussian distribution is assumed, the calculated Fresnel reflection coefficient, R_0, deviates significantly from the known value of –2.1 dB (0.61). In contrast, when a more peaked Laplacian distribution function is used, the calculated R_0 is much closer to the expected value (0.61). Based on this result, he suggests that under conditions of very low surface wind speeds, the slopes of the surface roughness depart rather markedly from the universally assumed Gaussian form. Chapron et al. (2000) also present analysis of compounded random processes causing non-Gaussian distribution of the surface roughness. A noticeable example is the modulation of small-scale waves by long waves. In which case, the random phase assumption is no longer valid and an enhanced peakedness in the pdf may occur.

In summary, it is noted that the procedures described in Sections 3.5.3.1 and 3.5.3.2 stress the nonlinear properties of the surface waves or radar wave-surface wave interaction. Because nonlinearity of ocean waves increases with wind speed, one would expect that the data scatter of altimeter cross sections increases with wind speed as more processes (e.g., breaking, foam, whitecaps, nonlinear surface geometries) enter the scattering process in high wind conditions. As shown in Figs. 7(b) and 9, the variability of σ_0 is in fact decreasing monotonically toward high wind speeds. This trend is a characteristic feature of ambient attenuation (Fig. 9). It is concluded that the observations of enhanced cross-section variability and discrepancy between analytical calculations and measurements at mild-to-moderate wind speeds can be explained by the attenuation effect due to ambient roughness.

3.6 Conclusions

The altimeter backscattering cross section is related to surface wind speed through the connection of ocean surface roughness. When disagreements between computations and measurements occur, the main focus of many earlier studies is on the nonlinearities in the scattering system, including surface wave processes (such as wave breaking and nonlinear geometry) and interaction of radar wave and surface wave. In principle, these efforts benefit model-data agreement in the high wind region where nonlinearity is more pronounced.

The analysis of altimeter measurements shows that it is in the mild-to-moderate wind speed range (U_{10}<~7 m/s) where analytical calculations deviate severely from data. Also, the variability of altimeter

cross sections is in fact much higher in the mild-to-moderate wind speed range. These are surprising observations because mild and moderate wind conditions represent a more benign environment for theoretical treatment. The large variability and severe model-data discrepancies of altimeter cross sections in the mild-to-moderate wind conditions cannot be explained by the nonlinearities in the scattering system.

In the ocean, there are always disturbances on the ocean surface caused by some background fluctuations that are not related to local wind conditions. Obvious examples include swell from distant storms and surface disturbances caused by turbulent motions of ocean currents. As a result of the ambient roughness, an attenuation factor of the form of $\Delta\sigma_{1D}=[(s_f+2s_t)/(s_f+2s_t+S)]^{1/2}$ or $\Delta\sigma_{2D}=s_{ft}/(s_{ft}+S)$ enters into the equation relating the scattering cross section and surface roughness. For a given level of ambient roughness, the attenuation increases monotonically toward lower wind speeds. The wind speed dependence of the ambient attenuation is identical to that of the altimeter cross-section variability (Fig. 9(b)) and explains the observed increasing discrepancy between measurements and analytical solutions (that do not consider ambient attenuation) toward mild and moderate wind conditions (Fig. 14(a)).

To address the sea state influence on the ambient parameter, data from the Bering Sea and the Gulf of Alaska are analyzed. Through an empirical optimization approach, a set of formulas (Eqs. (22-25)) is recommended for the wind speed algorithm considering ambient roughness. From statistical comparison of measured and calculated σ_0, analytical solutions incorporating ambient roughness yield excellent agreement with the TOPEX altimeter measurements. The proposed ambient roughness function is tested with other independent datasets collected in the Gulf of Mexico and near Hawaii. The agreement between calculated results and measurements is also excellent.

4. WIND SPEED RETRIEVAL FROM ALTIMETER RETURNS CONSIDERING AMBIENT ROUGHNESS

4.1 Background

Radar sea returns are related to wind speeds through the ocean surface roughness, mainly attributed to wind-generated surface waves in the ocean. Using satellite altimeter output, sea surface wind speed can be obtained every 7 km along a groundtrack. Comparisons with in situ buoy measurements show that the accuracy of altimeter wind measurements is approximately 1.8 m/s over the global scale, and close to 1.2 m/s in a low sea state region (e.g., Brown 1978, 1981, 1990; Brown et al. 1981; Chelton and Wentz 1986; Dobson et al. 1987; Witter and Chelton 1991; Wu 1992; Ebuchi and Kawamura 1994; Freilich and Challenor 1994; Gower 1996; Hwang et al. 1998). The measured radar intensity (the normalized radar cross section), σ_0, however, is found to differ significantly from theoretical calculations (e.g., Brown 1990). Up to this date, the operational wind speed algorithms are based on empirical or statistical correlation derived from collocated and simultaneous measurements from in situ buoys and spaceborne altimeters.

Hwang et al. (1997, 1998) investigate the attenuation of the radar cross section due to waves much longer than the radar wavelength. Their analysis produces a solution that results in much better agreement with in situ measurements. The rms wind speed difference between buoy and altimeter data is reduced by more than 40 percent. Further analysis (Section 3) reveals that the impressive performance is attributed to incorporating ambient roughness in their solution. Two primary contributors of the ambient component are fluctuations due to turbulence processes that are not related to local wind conditions and swell that are originated in distant regions. Using the dataset acquired in the Bering Sea and in the Gulf of Alaska, the sea state influence on the ambient roughness S is investigated in Section 3. Empirical functions of $S(U_{10}, H_s)$ are presented, where U_{10} is the neutral wind speed at 10 m elevation and H_s is the significant wave height.

The influence of the significant wave height on the altimeter return at a given wind speed has been noted since the late 1980s. Earlier efforts to incorporate wave height parameters into the altimeter wind speed algorithms include multiple regressions (Monaldo and Dobson 1989; Lefevre et al. 1994) and introduce a wave age dependence on the altimeter return (Glazman and Greysukh 1993). The former approach uses the altimeter output and reference datasets (e.g., collocated buoy measurements or wind speeds from other satellite sensors) to establish a bivariable dependence of wind speed on the altimeter cross section and significant wave height; the latter eventually derives a pseudo wave age using the altimeter outputs of wind speed and significant wave height. There appear to be improvements in these two-parameter algorithms but the comparisons with in situ data are not conclusive. A more extensive discussion of these efforts is given in Lefevre et al. (1994).

In this section, collocated and simultaneous altimeter and buoy data in the Bering Sea and the Gulf of Alaska are compiled to investigate the sea state effects on wind speed retrieval from altimeter measurements. As described in Section 3, the ranges of wind speeds and wave heights in these datasets are much wider than that of the Gulf of Mexico dataset. The altimeter return is noticeably reduced with increasing wave heights. Such sea state influence is consistent with the results reported by Anderson et al. (1999) and Gourrion et al. (2000). Section 4.2 presents a brief summary of the functional relation between altimeter signal attenuation and ambient roughness. Section 4.3 describes an iteration procedure that takes into account the ambient roughness and sea state influence to retrieve wind speeds from altimeter returns. The iteration procedure is an operational algorithm and requires only the altimeter outputs (radar cross section and significant wave height) for the derivation of wind speeds. Compared with the results derived from standard operational algorithms, e.g., MCW (Witter and Chelton 1991) or SB (Brown et al. 1981), the comparison statistics of the iteration procedure are comparable or better. The probability distribution function (pdf) of the derived wind speeds using the iteration procedure is also much closer to the pdf of the buoy dataset, as illustrated in the first four moments of the pdf. The iteration procedure achieves about 10 percent improvement in the statistics of rms difference, but still much less than the 40 percent potential improvement according to the forward computation result. Section 4.4 discusses issues of wind speed functions of the mean square slopes. In particular, it is found that in order to achieve a better comparison with buoy measurements, in the iterative procedure (to obtain wind speed from altimeter outputs), it is necessary to prescribe a higher mean square slope function than the one used for the forward computation (to calculate altimeter cross section and attenuation knowing wind speed). This is because the altimeter backscattering process is a multiple-inputs system, in which wind-induced roughness and ambient roughness are the two main inputs. At the present stage, the best functional representation of the ambient roughness requires wind speed input. As this is not available from the original altimeter outputs, the initial guess of wind speed from the iteration procedure is contaminated by the unknown ambient roughness. The contamination can be mitigated by artificially elevating the wind-induced surface roughness. Finally, Section 4.5 presents the summary and conclusions.

4.2 Altimeter Cross Sections and Surface Roughness

The trend of enhanced attenuation of altimeter returns with increasing sea state as illustrated in Figs. 6 and 7 is consistent with the analysis of attenuation caused by ambient roughness (Section 3). An equation relating the altimeter backscattering cross section and surface roughness components is given by Eq. (13) (Hwang et al. 1998). If a 2D Gaussian distribution is applied, the solution is Eq. (15). Equation (15) is identical to the familiar lowest order solution relating the altimeter cross section and the filtered roughness (e.g., Barrick 1968; Brown 1978) if the ambient roughness is not considered, that is, $S = 0$,

$$\sigma_{00} = \frac{R_0}{s_{ft}}, \tag{27}$$

where s_{ft} is the total filtered surface roughness contributing to altimeter backscatter; by definition, $s_{ft} = s_f + s_t$. Hwang et al. (1997) consider the surface roughness as the sum of sinusoidal waves on the ocean

surface. The half wavelength $\lambda/2$ represents the length scale that the surface feature changes from a convex to a concave geometry. The dimensionless length scale of the surface geometry for scattering consideration is thus expressed as $R = k_r\lambda/2$, where k_r is the radar wavenumber. The portion of the surface wave spectrum within $1 \le R \le 50$ is designated as the short-scale filtered mean square slope component, and the portion of $R > 50$ the long-scale component. Using the spectral model proposed by Hwang (1997), the wind-induced slope components are calculated by

$$s_f = 3.66\times10^{-3}U_{10}, \tag{28}$$

and

$$s_t = 1.09\times10^{-3}U_{10} + 1.25\times10^{-3}. \tag{29}$$

Based on these formulas, a forward computation method is described by Hwang et al. (1997, 1998). The ambient attenuation factor $\Delta\sigma$, taken as the square root portion on the right-hand side of Eq. (13), is

$$\Delta\sigma_{1D} = \sqrt{\frac{s_f}{s_f + 2v_t}}, \tag{30}$$

where subscript 1D represents solutions with 1D Gaussian assumption of the surface slopes of long scale waves. The attenuation factor can be calculated from the buoy wind speed and an empirically determined $S = 0.02$. This attenuation factor is removed from the measured cross section σ_0. The resulting $\sigma_{001D} = \sigma_0/\Delta\sigma_{1D} = R_0/s_f$ is then used to calculate the filtered mean square slope s_f and to derive the wind speed, U_{10}, from Eq. (28).

In practice, it is found that for the forward computation, a better agreement between altimeter and buoy measurements of wind speeds can be achieved if the dependence of the mean square slope components on wind speed is modified to be Eqs. (20 and 21). The wind speed derived from this forward computational procedure is in excellent agreement with the buoy measurement. An improvement of 40% in the rms difference over the operational algorithms is found for the Gulf of Mexico dataset (Table 4 of Hwang et al. 1998). Additional discussions on these two sets of wind speed functions (Eqs. (28 and 29) and (20 and 21)) are presented in Section 3.

In a similar fashion, for the 2D Gaussian assumption (Eq. (15)), the attenuation factor can be calculated by

$$\Delta\sigma_{2D} = \frac{s_{ft}}{s_{ft} + S}. \tag{31}$$

Similarly, from experiment, the mean square slope components calculated using Eqs. (20 and 21) with a reduced level of ambient roughness ($S = 0.015$) produce best results. The same forward computation is applied to the Gulf of Alaska and Bering Sea datasets for both 1D and 2D assumptions, denoted as F1D and F2D, respectively. The results are plotted in Fig. 16(a-b). The statistics of comparison with buoy data, including bias, regression coefficient, rms difference, and correlation coefficient, are listed in Table 5. For reference, the statistics of TOPEX-Buoy comparison with four operational algorithms [MCW, SB, and two iteration algorithms further described in Section 4.4] are also tabulated in Table 5.

Table 5 — Basic Statistics of Comparison Between Calculated and Measured Wind Speeds

Algorithm	Bias (m/s)	Regression Coefficient	RMS (m/s)	Correlation Coefficient
Forward 1D (F1D), Low mss, S=0.02	0.026	0.983	1.172	0957
Forward 2D (F2D), Low mss, S=0.015	-0.078	0.979	1.075	0.962
Forward 1D (F1D), Low mss, $S_{lo}(U_{10},H_s)$	-0.013	1.002	0.942	0972
Forward 2D (F2D), Low mss, $S_{lo}(U_{10},H_s)$	0.119	1.015	0.913	0.974
MCW	0.595	1.066	1.794	0.910
SB	0.096	0.981	1.698	0.905
Iteration 1D (I1D)	-0.086	0.979	1.607	0.912
Iteration 2D (I2D)	-0.350	0.941	1.704	0.906

The scatter plots of the four operational algorithms are shown in Fig. 16(c-f). On average, the rms difference from the forward computations is about 40 percent better than the MCW results. Similar improvements are also shown in the statistics of bias, regression coefficient, and correlation coefficient. The excellent results of the forward computations suggest that the agreement of altimeter measured wind speed and analytical computation is much better than previously believed, and that a significant improvement of wind speed retrieval from altimeter cross section is possible. The rms differences between measured and forward-calculated wind speeds are 1.08 (2D) and 1.17 (1D) m/s, while the rms of the four operation algorithms ranges between 1.61 and 1.79 m/s. Similar improvements in bias, regression coefficient, and correlation coefficient are also likely (Table 5).

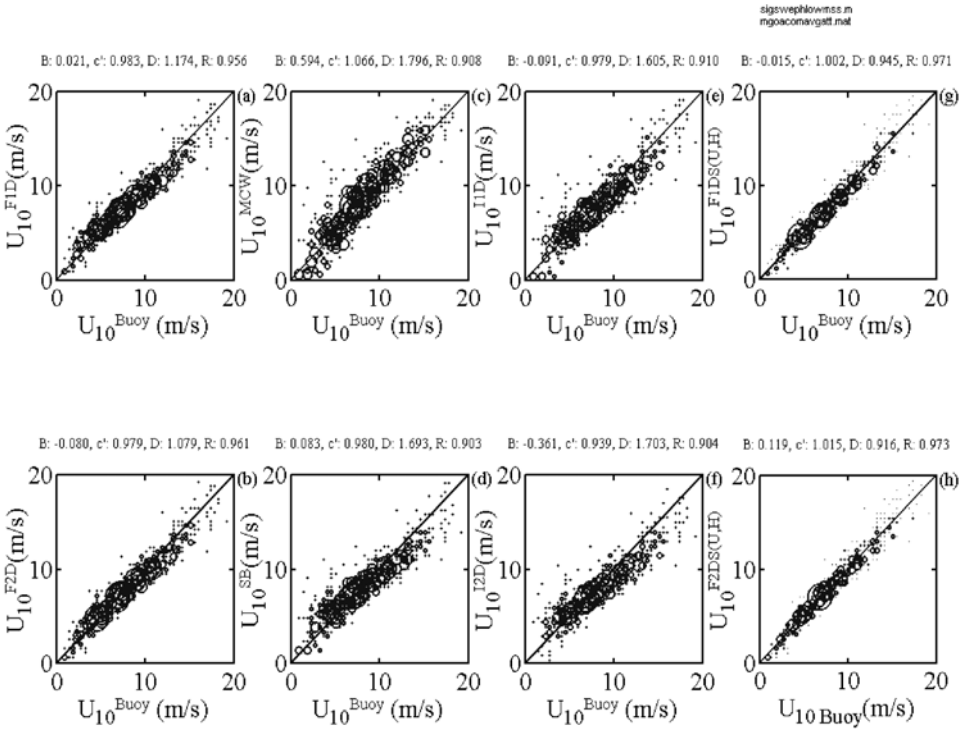

Fig. 16 — A comparison of (buoy) measured and calculated wind speeds using different operational algorithms. (a) F1D, S = 0.02, (b) F2D, S = 0.015, (c) MCW, (d) SB, (e) I1D, (f) I2D, (g) F1D, $S_{lo}(U_{10},H_s)$, and (h) F2D, $S_{lo}(U_{10},H_s)$.

4.3 Iterative Algorithms

An operational algorithm for wind speed from the altimeter cross section, taking into consideration the ambient roughness effect, is derived from Eqs. (13), (28), and (29) (Hwang et al. 1998),

$$U_{10} = \frac{-K_2 + \sqrt{K_2^2 + 4K_1K_3}}{2K_1} \quad , \qquad \text{(1D)} \tag{32}$$

where $K_1 = B_1^2 + 2B_1B_2$, $K_2 = 2B_1(B_3+S)$, and $K_3 = (R_0/\sigma_0)^2$, and B_1, B_2, and B_3 are the coefficients relating the mean square slope components to the wind speed, $s_f = B_1U_{10}$ and $s_t = B_2U_{10}+B_3$. For applications to the Ku-band, $B_1 = 3.66 \times 10^{-3}$, $B_2 = 1.09 \times 10^{-3}$, and $B_3 = 1.25 \times 10^{-3}$ (Eqs. (31-32)). In Hwang et al. (1998), $S = 0.02$ is determined empirically based on the Gulf of Mexico dataset.

With the 2D solution, an operational algorithm can be derived from Eqs. (15), (28), and (29),

$$U_{10} = \frac{1}{(B_1 + B_2)}\left(\frac{R_0}{\sigma_0} - S - B_3\right) . \qquad \text{(2D)} \tag{33}$$

Hwang et al. (1998) suggest that an empirical formula with wind speed dependence on S may improve the accuracy of wind speed retrieval from the altimeter cross section. Because σ_0, U_{10} and S are dependent variables, connected through the scattering equation, Eq. (13) or (15), and the correlation of wind speed and surface roughness, Eqs. (28 and 29) or Eqs. (20 and 21), the properties of the ambient roughness can be analyzed from collocated measurements of altimeter cross sections and sea state information from buoys. This is done in Section 3 using the data collected in the Bering Sea and the Gulf of Alaska. The functional form that provide optimal agreement between measured and calculated altimeter cross sections (using Eqs. (28 and 29) for the mean square slope components) is given by

$$S = S_0 f_1(U_{10}) f_2(H_s, U_{10}) + f_3(H_s) , \tag{34}$$

with the following functions,

$$f_1(U_{10}) = \left\{1 - \left(\frac{U_{10}}{B_U}\right)^{\alpha_1}\right\}^{\beta_1} , \tag{35}$$

$$f_2(H_s, U_{10}) = B_{HU} H_s^{\alpha_2\left[1-\left(\frac{U_{10}}{B_U}\right)^{\alpha_1}\right]}, \tag{36}$$

and

$$f_3(H_s) = B_H H_s^{\alpha_3} . \tag{37}$$

The two sets of eight coefficients in Eqs. (34-37) for the 1D and 2D solutions are determined empirically, and listed in Table 6.

Table 6 — Parameters Used in Defining the Functions of S

	S_0	α_1	β_1	α_2	α_3	B_U	B_{HU}	B_H
1D	0.02	0.3	1.08	0.5	0.5	20	2.75	0.0008
2D	0.012	0.4	1.2	1.15	0.1	20	1.3	0.005

Equations (34-37) are very similar to Eqs. (22-25) given in Section 3, which uses Eqs. (20 and 21) for the mean square slope components (low mss), and the ambient roughness (represented by S_{00}) needs to increase to a constant level of 0.0075 for the 1D solution, and to 0.0035 for the 2D solution (Eqs. (22 through 25). As predicted by Hwang et al. (1998), the agreement between computed and measured wind speeds is further improved with the functional form representation of the ambient roughness (Table 5 and Fig. 16(g-h)).

Given the function $S(U_{10}, H_s)$, an iteration procedure can be developed to improve wind speed retrieval from altimeter cross sections by incorporating the effect of ambient attenuation. A constant $S = S_{init}$ is used to obtain the initial estimate of the wind speed from Eq. (32) or (33). From experiment, $S_{init} = 0.02$ for 1D and $S_{init} = 0$ for 2D yield very good results. The improvement through the iteration process is shown in Table 7. The statistics of the 2D case are italicized and the best results up to four iterations are shown in boldface.

Table 7 — Statistics Showing Improvement of the Iteration Algorithms

	Bias (m/s)		**Regression Coefficient**		**RMS (m/s)**		**Correlation Coefficient**	
	1D	*2D*	1D	*2D*	1D	*2D*	1D	*2D*
Initial estimate	-0.846	*1.588*	0.873	*1.129*	1.960	*2.359*	0.906	*0.904*
Iteration 1	-0.243	***-0.350***	0.958	***0.939***	1.634	***1.704***	0.910	***0.906***
Iteration 2	-0.117	*-0.701*	0.975	*0.912*	1.610	*1.820*	0.911	*0.903*
Iteration 3	-0.091	*-0.778*	0.979	*0.906*	1.607	*1.836*	0.912	*0.905*
Iteration 4	**-0.086**	*-0.811*	**0.979**	*0.905*	**1.607**	*1.868*	**0.912**	*0.902*

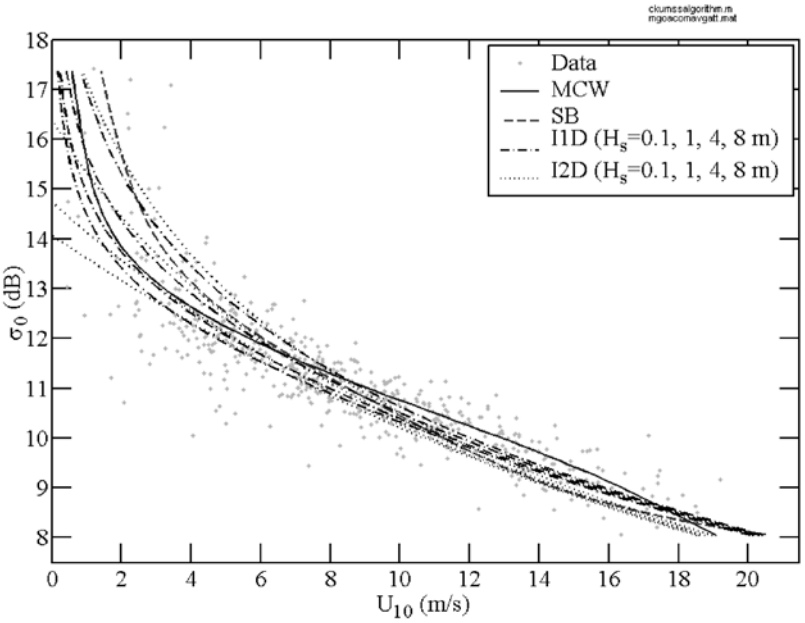

Fig. 17 — A comparison of calculated altimeter cross sections as a function of buoy wind speed. The iterative procedures are shown for H_s = 0.1, 1, 4, and 8 m (higher H_s results in lower σ_0 in each set of curves). The measured altimeter cross sections are shown by dots.

For the 1D solution, the iteration procedure continues to improve as the iteration number increases. For the 2D solution, the best results are achieved at the first iteration. Similar results are obtained using different datasets (e.g., Gulf of Mexico). In the subsequent discussions, the solutions of the fourth iteration for 1D and the first iteration for 2D are used.

On comparing the iteration results (Table 7) with the corresponding statistics of MCW and SB in Table 5, the performance of the iteration algorithms is comparable to that of the MCW in one iteration, and for the 1D solution, the procedure achieves incremental improvement for each additional iteration. The resulting $\sigma_0(U_{10})$ calculated from the MCW, SB, I1D, and I2D are plotted in Fig. 17. The collocated buoy and TOPEX data are also shown as dots. Curves of the iteration algorithms calculated for H_s = 0.1, 1, 4, and 8 m pass through the data cluster and follow the general data trend very well, reflecting the good statistics shown in Table 5.

The pdf and the error trend of the computed and measured wind speed differences, ΔU, are presented in Figs. 18 and 19. The pdf of ΔU for the four operational algorithms are similar. Least square fitting of $\Delta U(U_{10})$ produces

$$\Delta U_{MCW} = -0.055U_{10} + 1.067\,, \tag{38}$$

$$\Delta U_{SB} = -0.257U_{10} + 2.277\,, \tag{39}$$

$$\Delta U_{I1D} = -0.153U_{10} + 1.218\,, \text{ and} \tag{40}$$

$$\Delta U_{I2D} = -0.233U_{10} + 1.634\,. \tag{41}$$

These least square curves are shown in Fig. 19, together with the scatter plots of ΔU vs U_{10}. The error trend of MCW is clearly the best of the four, followed in sequence by I1D, I2D, and SB.

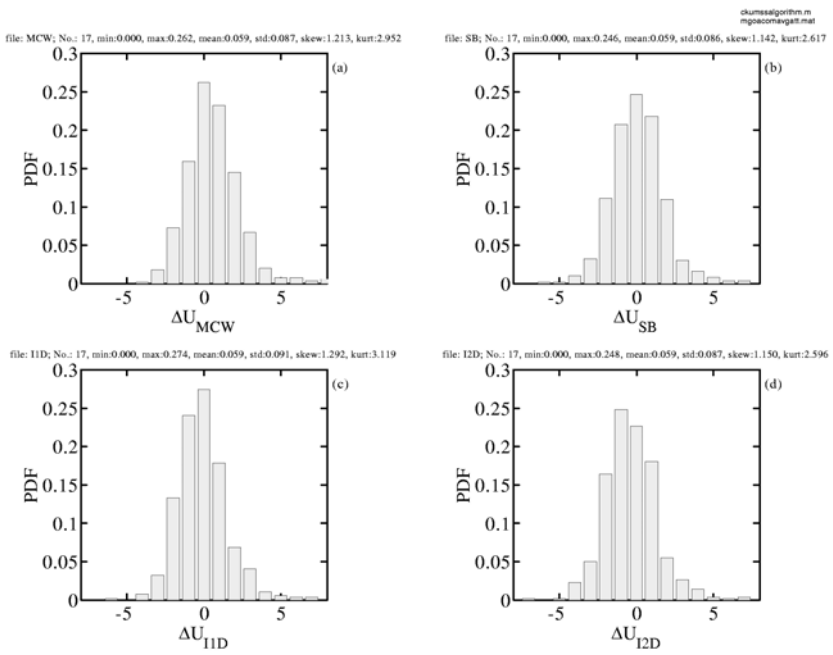

Fig. 18 — Pdf of the calculated and measured wind speed difference ΔU

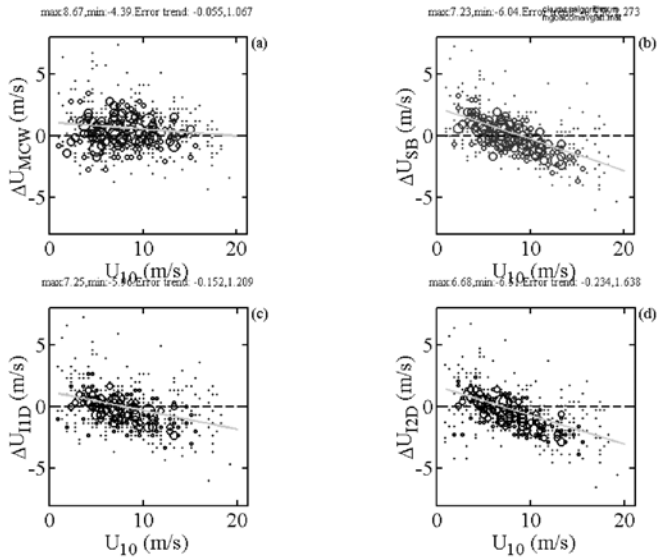

Fig. 19 — Scatter plots of ΔU vs U_{10}, (a) MCW, (b) SB, (c) I1D, and (d) I2D. The solid curve in each panel is the linear error trend derived from least square fitting.

Finally, we compare the pdf of (buoy) measured and calculated wind speeds (Fig. 20(a)). The distribution of buoy measured wind speeds is approximately Rayleigh. The SB results are more narrowly distributed and the mode of distribution biases high. The I2D distribution is also much narrower than the buoy data but produces the correct mode of the distribution function. The MCW and I1D yield distributions in better agreement with the buoy data, with MCW been slightly broader, and the I1D slightly narrower. The mode of distribution is correctly represented by the wind speeds derived from the I1D procedure. The first four moments of the distributions function,

$$m_1 = \frac{\int U_{10} p(U_{10}) dU_{10}}{\int p(U_{10}) dU_{10}}. \tag{42}$$

and

$$m_n = \frac{\int (U_{10} - m_1)^n p(U_{10}) dU_{10}}{\int p(U_{10}) dU_{10}}, \; n=2, 3, 4, \tag{43}$$

are tabulated in Table 8.

Table 8 — The First Four Moments of Wind Speed Pdf

	m_1	m_2	m_3	m_4
Buoy	8.444	15.23	24.19	600.8
MCW	9.067	16.65	11.69	680.8
SB	8.586	10.84	15.53	418.5
I1D	8.405	13.51	24.40	581.8
I2D	8.165	10.88	13.65	384.3
Normalized				
MCW/Buoy	1.074	**1.093**	0.483	1.133
SB/Buoy	1.117	0.712	0.642	0.697
I1D/Buoy	**0.954**	0.869	**1.008**	**0.969**
I2D/Buoy	0.967	0.715	0.564	0.640

The overall performance of the I1D is better than the other three algorithms. The first four moments of the pdf normalized by the buoy results are 0.954, 0.867, 1.008, and 0.969 (with 1.0 represents perfect agreement). The difference of the calculated and measured pdf is shown in Fig. 20(b). The rms differences are 0.023, 0.038, 0.022, and 0.033 for MCW, SB, I1D, and I2D, respectively. The MCW and I1D perform equally well in this category and are slightly better than the other two algorithms. The frequency of occurrences at low wind speed range is underestimated by all algorithms, and the largest deviation of analytical algorithms (SB, I1D, I2D) occurs in the wind speed range just above the mode of distribution.

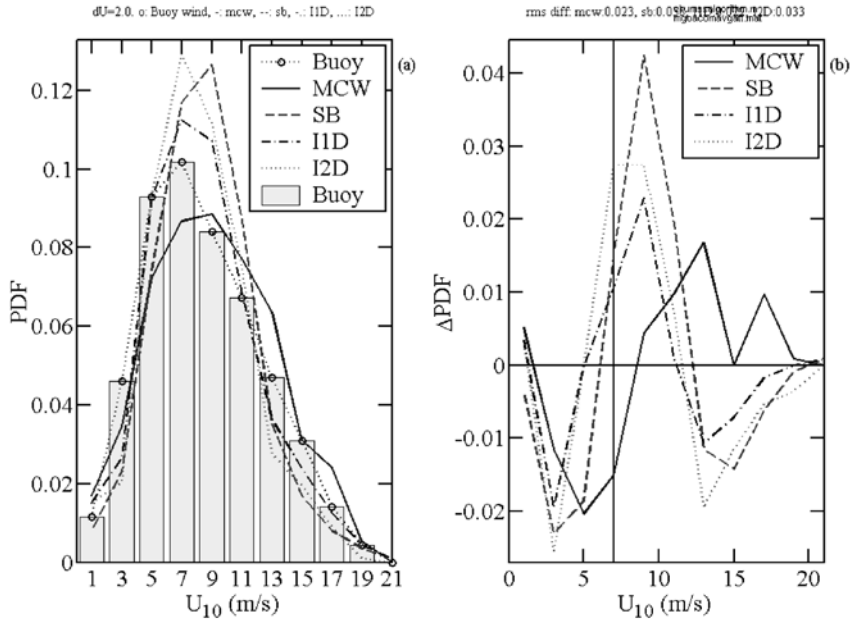

Fig. 20 — (a) PDF of the calculated and measured wind speeds; (b) the difference between the calculated and measured pdf.

4.4 Discussions

The performance of the I1D algorithm is comparable to or better than the operational algorithms now being used as the standard procedure to retrieve wind speeds from altimeter cross sections. Using the MCW results as reference, I1D improves the rms difference about 10 percent (from 1.79 m/s to 1.61 m/s). This is a positive development as the iteration procedure is based on an analytical solution of altimeter scattering taking into account the ambient attenuation effect, rather than an empirical correlation derived from collocated buoy and altimeter datasets. As an analytical solution, it is expected that the accuracy of the solution will continue to improve as our understanding of the sea surface properties continues to advance. The iteration procedure, however, still does not achieve the accuracy expected from the forward computation procedure, which suggests that the rms error of the altimeter wind measurement is less than 1 m/s, or more than 40 percent better than the MCW results (Table 5). At this stage, two major obstacles for achieving the full potential of the altimeter wind speed accuracy are the wind speed function of the surface roughness and the characteristics of ambient roughness. Some comments on these two topics are presented in the following.

4.4.1 Wind-induced Surface Roughness

It is emphasized that the forward computation is a research algorithm rather than an operational algorithm. Because the procedure as formulated requires *a priori* knowledge of the long scale and short scale surface roughness components, the results shown in Fig. 16(a,b) make use of the buoy-measured surface wind speed to calculate the wind-induced and ambient roughness components. The primary purpose of the forward computation is to illustrate that if the ambient attenuation can be accounted for, wind speeds measured by satellite altimeters are in much better agreement with in situ measurements. Retrieving wind speed to the full capability of the altimeter, however, remains a challenge. The iteration procedure and the forward calculation consider essentially the same ambient attenuation effect relating σ_0 and U_{10}. The difference in the outcome of the two procedures is obviously caused by the direction of applying the computation of the ambient attenuation factor. In particular, a significantly better agreement is found in the forward procedure that derives the attenuation factor knowing U_{10}. Figure 21(a) shows the scatter plot of σ_0 and U_{10} for a typical altimeter-buoy dataset. The calculated ambient attenuation, $\Delta\sigma$, is plotted as a function of U_{10} in Fig. 21(b), and as a function of σ_0 in Fig. 21(c). All three plots deliver the same message that the spreading of $\Delta\sigma$ as a function of σ_0 is much wider compared to the spreading of $\Delta\sigma$ as a function of U_{10}. For example, the cross section variability is typically 2 dB over a broad range of wind speeds (Fig. 21(b)), the variability increase to 3 to 4 dB when evaluated from σ_0 (Fig. 21(c)). In the iteration procedure, the initial estimate of wind speed relies on the altimeter cross section, which is a combined result of at least two major inputs (the wind-induced roughness and the ambient roughness, both are unknown at the first step of iteration). The error of the initial wind speed estimated from the altimeter cross section causes a less effective correction of the ambient attenuation. In practice, it is necessary to prescribe a higher mean square slope as a function of wind speed to account for the ambient attenuation of the altimeter cross section (Section 3). Iteration procedures that are applied with low mss functions (Eqs. (20-21)) produce very poor results (rms difference> 2 m/s, bias > 1 m/s).

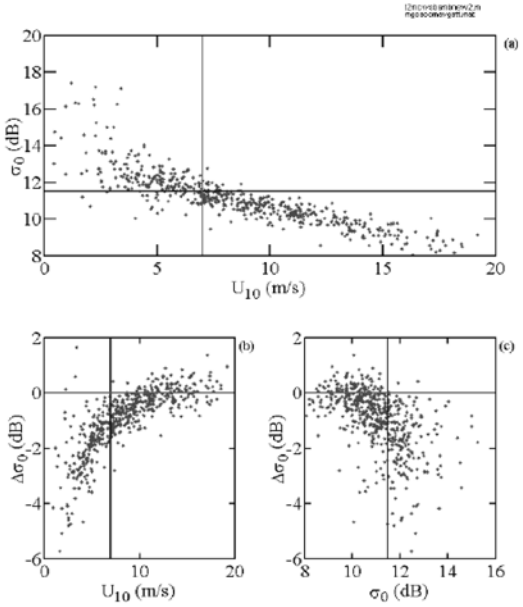

Fig. 21 — (a) Scatter plot of radar cross sections and wind speeds. (b) Calculated attenuation factor of the altimeter backscattering cross section $\Delta\sigma$ as a function of wind speed. (c) Same as (b) but plotted against the radar cross section. Solid lines are drawn as visual aid for comparing $\Delta\sigma(U_{10})$ with $\Delta\sigma(\sigma_0)$.

4.4.2 Ambient Parameter

Hwang et al. (1997, 1998) introduce an ambient parameter S as a part of the long wave slope component. In Hwang et al. (1998) a constant empirical value of 0.02 is used. The magnitude of S can be estimated from the consideration of wave stability. For a periodic wave train, it has been established that the maximum ratio of wave height to wavelength is 1/7 for deepwater waves (Michell 1893; Longuet-Higgins and Fox 1977), corresponding to a steepness (defined as the product of wavenumber K and wave amplitude $H/2$) of $\pi/7$. The mean square slope of a sinusoidal wave train with maximum slope is then $(\pi/7)^2/2 = 0.10$, representing the maximum value of S.

Although NDBC buoys are operational buoys with a cutoff frequency of 0.4 Hz (wavelength 10 m), their standard output of the average period, T_a, and significant wave height, H_s, may be used to estimate the ambient parameter. The buoy-measured mean square slope is calculated by $S_b = (K_a H)^2/8$, where K_a is calculated from T_a using the deep water dispersion relationship. The relationship of the attenuation factor ($\Delta\sigma$) with S_b is shown in Fig. 22 for wind speed bins of U_{10} = [0, 2], [2, 4], …, [18, 20] m/s. There is a strong dependence of $\Delta\sigma$ on S_b. For the data in each wind speed bin, $\Delta\sigma$ decreases 1 to 2 dB toward higher S_b. The magnitude of $\Delta\sigma$ tends to level off when S_b is small, indicating the absence of swell and other ambient waves. In addition, the dependence of $\Delta\sigma$ as a function of U_{10}, and therefore of s_f, is evident in this plot. Such dependence on the long wave steepness and wind speed is expected from the ambient attenuation effect (Section 3).

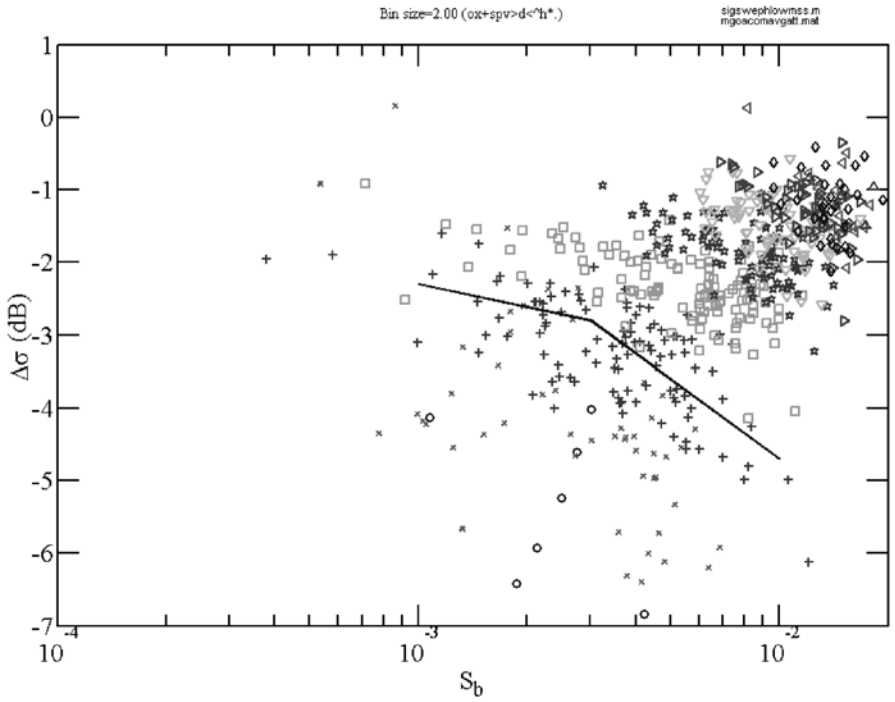

Fig. 22 — Altimeter attenuation as a function of mean square slope of long waves measured by buoys. Symbols represent different wind speed ranges (o: $0<U_{10}\leq 2$, ×: $2<U_{10}\leq 4$, +: $4<U_{10}\leq 6$, □: $6< U_{10}\leq 8$, ★: $8<U_{10}\leq 10$, ∇: $10<U_{10}\leq 12$, ▷: $12<U_{10}\leq 14$, ◇: $14<U_{10}\leq 16$, ◁: $16<U_{10}\leq 18$, △: $18<U_{10}\leq 20$ m/s). Two line segments are drawn to indicate the general trend of the data within each wind speed range.

Rather large S_b values exist even in the lower wind speed data (Fig. 22). Values as large as 7×10^{-3} are observed in the subset with $U_{10}<4$ m/s. The expected wavelengths at the spectral peaks of these low wind cases are less than 10 m and too short for the dynamic range of the buoy system (0.4 Hz maximum frequency). Therefore, for these low wind cases the wave properties measured by the buoy are predominantly ambient waves that are not locally generated. However, operational buoys are not designed to measure wave slopes. For example, the maximum value of S_b shown in Fig. 22 is less than 0.02 at U_{10} = 20 m/s, where breaking undoubtedly occurs. The mean square slope of waves at the breaking limit is 0.1. Studies of breaking waves have shown that it is a difficult task trying to derive mean square wave slopes or the acceleration parameters (both are related to the fourth moment of the wave spectrum) using surface buoy data (e.g., Snyder et al. 1983; Hwang et al. 1989). It is reasonable to state that S_b represents an underestimation of S (possibly by a factor between 5 and 10). Even with these reservations, it is quite encouraging to find that the functional dependence of the attenuation factor on the wind speed and large-scale surface slopes as displayed in Fig. 22 are in good agreement with the prediction of the roughness attenuation mechanism.

4.5 Conclusions

Field data show that for a given wind speed, the altimeter backscattering cross section decreases with increasing wave height (Figs. 7, 8, and 17). The magnitude of this sea state attenuation decreases toward higher wind speeds. This trend is consistent with the attenuation mechanism of altimeter scattering due to the presence of ambient roughness (Section 3). An analytical solution (Eq. (32)) incorporating the ambient attenuation mechanism to derive wind speed from altimeter cross section is developed by Hwang

et al. (1998). The solution is based on the 1D Gaussian assumption of long wave slopes. For the 2D Gaussian assumption, the corresponding solution is Eq. (33).

Hwang et al. (1998) assume a constant value for the ambient parameter ($S = 0.02$). They suggest that a functional form of $S(U_{10})$ may provide significant improvement in the wind speed retrieval. As U_{10} is not available in the initial altimeter dataset, an iteration procedure is developed in this Section. The procedure takes into account the sea state influence of the ambient roughness and uses the functional form of $S(U_{10},H_s)$ developed in Section 3. Using MCW algorithm as reference, the I1D procedure performs better in the statistics of bias, regression coefficient, rms difference and wind speed pdf; comparable in correlation coefficient; and not as good in the error trend of the wind speed difference (Tables 5, 7, Fig. 16, Eqs. (38-41)). The 1-D iteration procedure (I1D) yields 10 percent improvement in the resulting rms wind speed difference, and a similar level of improvement in other key statistics such as bias, regression coefficient, and correlation coefficient. More importantly, the iteration procedure is a semi-analytical algorithm, which will continue to improve as our understanding of the ocean surface roughness properties (both wind-induced and ambient components) advances. The results presented here also suggest that the predominant effect of sea state influence on the altimeter return is the scattering attenuation from ambient roughness rather than the hydrodynamic modulation or modification of the wind-induced roughness by the sea state parameters.

5. SUMMARY

To properly interpret ocean remote sensing measurements, it is necessary to have an accurate understanding of the ocean surface roughness. Triggered by the curious result of the huge difference between the mean square roughness measured in clean and slicked waters (Cox and Munk 1954), and the drastic differences among the spectral models created to explain the large differences, we set out to investigate the possibility of deriving mean square roughness from the active sensor of a spaceborne altimeter. Through this pursuit, it is realized that ambient roughness exists in the absence of wind events. The analytical computation of altimeter cross sections incorporating the ambient roughness is in significantly better agreement with measured data as compared to computations that neglect the ambient roughness. From this understanding, a technique is developed to derive the wind-induced ocean surface roughness from collocated altimeter and buoy data using the upper bound of $\sigma_0(U_{10})$ data clusters. The result resolve a long-standing puzzle in earlier publications showing the roughness derived from radar to be larger than that obtained by optical methods.

The wind speed dependence of the surface roughness derived from the altimeter is basically similar to that of the optical results. Both show exceedingly higher mean square roughness than can be accounted for by extending the saturation spectrum to the cutoff wavelength of the electromagnetic waves. The common practice is to introduce spectral models with much higher spectral densities at the short gravity wave region to match the Cox and Munk (1954) clean water results. It is not clear which generation mechanisms can produce such greatly enhanced spectral energy in the short gravity wave region.

In their classic paper, Cox and Munk (1954) document in great detail their field experiments and data analysis procedures. Their description that the slick surfaces remain coherent in conditions up to about 9 ms^{-1} provides a crucial clue suggesting that in addition to damping short waves, the artificial slicks they have laid out also suppressed wave break events. We propose that the large roughness differences between clean water and slicked conditions are primarily caused by the breaking waves rather than the reduced spectral range due to short wave damping. Based on the saturation spectrum function, extending spectral range only increases surface roughness logarithmically and cannot account for the large differences measured.

ACKNOWLEDGMENTS

The TOPEX data are provided by the National Aeronautics and Space Administration TOPEX/POSEIDON Project, the ocean buoy data are supplied by the National Data Buoy Center. Their generosities are gratefully appreciated. This work is sponsored by the Office of Naval Research.

REFERENCES

Anderson, C., J.T. Macklin, C. Gommenginger, M.A. Srokosz, P.G. Challenor, and V. Karaev, "Study of the Impact of Sea State on Nadir Looking and Side Looking Microwave Backscatter," *Tech. Note WP30*, Image Analysis Group, Marconi Research Center and Southampton Oceanography Centre, 1999.

Barrick, D.E., "Rough Surface Scattering Based on the Specular Point Theory," *IEEE Trans. Antennas Propag.* **AP-16**, 449-454, 1968.

Brown, G.S., "Backscattering from a Gaussian Distributed, Perfectly Conducting, Rough Surface," *IEEE Trans. Antennas Propag.* **AP-26**, 472-482, 1978.

Brown, G.S., "Surface Roughness Density Estimates for Low Sea State Conditions," *J. Geophys. Res.* **84**, 3987-3989, 1979.

Brown, G.S., "The Wind Speed Measurement Capability of Spaceborne Radar Altimeters," *IEEE J. Oceanic Eng*. **OE-6**, 59-63, 1981.

Brown, G.S., "Quasi-specular Scattering from the Air-sea Interface," in *Surface Waves and Fluxes,* Vol. 2, W. Plant and G. Geernaert, eds. (Kluwer Academic, Dordrecht, The Netherlands, 1990), pp. 1-40.

Brown, G.S., H.R. Stanley, and N.A. Roy, "The Wind Speed Measurement Capability of Spaceborne Radar Altimeters," *IEEE J. Oceanic Eng.* **OE-6**, 59-63, 1981.

Chapron, B., V. Kerbaol, D. Vandemark, and T. Elfouhaily, "Importance of Peakedness in Sea Surface Slope Measurements and Applications," *J. Geophys. Res*. **105**, 17195-17202, 2000.

Chelton, D.B. and F.J. Wentz, "Further Development of an Improved Altimeter Wind Speed Algorithm," *J. Geophys. Res*. **91**, 14250-14260, 1986.

Chelton, D.B., E.J. Walsh, and J.L. McArthur, "Pulse Compression and Sea Level Tracking in Satellite Altimeters," *J. Atm. Oceanic Tech.* **6**, 407-438, 1989.

Cox, C.S. and W. Munk, "Statistics of the Sea Surface Derived from Sun Glitter," *J. Mar. Res.* **13**, 198-227, 1954.

Cox, C.S. and W. Munk, "Slopes of the Sea Surface Deduced from Photographs of Sun Glitter," *Bull. Scripps Instit. Oceanogr., Univ. of Calif.* **6**, 401-488, 1956.

Dobson, E., F. Monaldo, J. Goldhirsh, and J. Wilkerson, "Validation of Geosat Altimeter-derived Wind Speeds and Significant Wave Heights Using Buoy Data," *J. Geophys. Res.* **92**, 10719-10731, 1987.

Ebuchi, N. and H. Kawamura, "Validation of Wind Speeds and Significant Wave Heights Observed by the TOPEX Altimeter Around Japan," *J. Oceanogr.* **50**, 479-487, 1994.

Freilich, M.H. and P.G. Challenor, "A New Approach for Determining Fully Empirical Altimeter Wind Speed Model Functions," *J. Geophys. Res*. **99**, 25051-25062, 1994.

Glazman, R.E. and A. Greysukh, "Satellite Altimeter Measurements of Surface Wind," *J. Geophys. Res.* **98**, 2475-2483, 1993.

Gourrion, J., D. Vandemark, S. Bailey, and B. Chapron, "Satellite Altimeter Models for Surface Wind Speed Developed Using Ocean Satellite Crossovers," Tech. Rep. *IFREMER-DROOS-2000-02*, 2000.

Gower, J.F.R., "Intercalibration of Wave and Wind Data from TOPEX/POSEIDON and Moored Buoy off the West Coast of Canada," *J. Geophys. Res.* **101**, 3817-3829, 1996.

Hara, T., E.J. Bock, and D. Lyzenga, "In Situ Measurements of Capillary-Gravity Wave Spectra Using a Scanning Laser Slope Gauge and Microwave Radars," *J. Geophys. Res.* **99,** 12593-12602, 1994.

Hara, T., E.J. Bock, J. Edson, and W. McGillis, "Observation of Short Wind Waves in Coastal Waters," *J. Phys. Oceanogr.* **28,** 1425-1438, 1998.

Hughes, B.A., H.L. Grant, and R.W. Chappell, "A Fast Response Surface Wave Slope Meter and Measured Wind-Wave Moment," *Deep- Sea Res.* **24**, 1211-1223, 1977.

Hwang, P.A., "A Study of the Wavenumber Spectra of Short Water Waves in the Ocean. Part 2. Spectral Model and Mean Square Slope," *J. Atm. Oceanic Tech.* **14**, 1174-1186, 1997.

Hwang, P.A., "Ambient and Breaking Roughness of the Ocean Surface," 2002 International Geoscience and Remote Sensing Symposium, *IEEE Conf. Proc.* **2**, 937-939, 2002.

Hwang, P.A., and O.H. Shemdin, "The Dependence of Sea Surface Slope on Atmospheric Stability and Swell Condition," *J. Geophys. Res*. **93**, 13903-13912, 1988.

Hwang, P.A. and D.W. Wang, "Directional Distributions and Mean Square Slopes in the Equilibrium and Saturation Ranges of the Wave Spectrum," *J. Phys. Oceanogr.* **31**, 1346-1360, 2001.

Hwang, P.A., D. Xu, and J. Wu, "Breaking of Wind-generated Waves: Measurements and Characteristics," *J. Fluid Mech.* **202**, 177-200, 1989.

Hwang, P.A., S. Atakturk, M.A. Sletten, and D.B. Trizna, "A Study of the Wavenumber Spectra of Short Water Waves in the Ocean," *J. Phys. Oceanogr.* **26**, 1266-1285, 1996.

Hwang, P.A., W.J. Teague, G.A. Jacobs, and D.W. Wang, "A Statistical Comparison of Wind Speed, Wave Height, and Wave Period Derived from Satellite Altimeters and Ocean Buoys in the Gulf of Mexico Region," *J. Geophys. Res.* **103**, 10451-10468, 1998.

Hwang, P.A., D.W. Wang, W.J. Teague, and G.A. Jacobs, "Effect of Surface Tilting on Altimeter Wind Measurement," Naval Research Laboratory NRL/MR/7332--97-8067, 1997.

Hwang, P.A., D.W. Wang, E.J. Walsh, W.B. Krabill, and R.N. Swift, "Airborne Measurements of the Wavenumber Spectra of Ocean Surface Waves. Part 1. Spectral Slope and Dimensionless Spectral Coefficient," *J. Phys. Oceanogr.* **30**, 2753-2767, 2000.

Jackson, F.C., W.T. Walton, D.E. Hines, B.A. Walter, and C.Y. Peng, "Sea Surface Mean Square Slope from Ku-Band Backscatter Data," *J. Geophys. Res.* **97**, 11411-11427, 1992.

Klein, L.A. and C.T. Swift, "An Improved Model for the Dielectric Constant of Sea Water at Microwave Frequencies," *IEEE Trans. Antennas Propag.* **AP-25**, 104-111, 1977.

Lefevre, J.M., J. Barckicke, and Y. Menard, "A Significant Wave Height Dependent Function for TOPEX/POSEIDON Wind Speed Retrieval," *J. Geophys. Res.* **99**, 25035-25049, 1994.

Longuet-Higgins, M.S., and M.J.H. Fox, "Theory of the Almost Highest Wave: the Inner Solution," *J. Fluid Mech.* **80**, 721-741, 1977.

Michell, J.H., "The Highest Wave in Water," *Phil. Mag.* **36**, 430-437, 1893.

Monaldo, F.M., and E.B. Dobson, "On Using Significant Wave Height and Radar Cross Section to Improve Radar Altimeter Measurements of Wind Speed," *J. Geophys. Res.* **94**, 12699-112701, 1989.

Phillips, O.M., "On Some Properties of the Spectrum of Wind-Generated Ocean Waves," *J. Mar. Res.* **16**, 231-240, 1958.

Phillips, O.M., *The Dynamics of the Upper Ocean*, 1st ed. (Cambridge U. Press, Cambridge, Great Britain, 1966).

Phillips, O.M., "Spectral and Statistical Properties of the Equilibrium Range in Wind-Generated Gravity Waves," *J. Fluid Mech*. **156**, 505-531, 1985.

Snyder, R.L., L. Smith, and R.M. Kennedy, "On the Formation of Whitecaps by a Threshold Mechanism. Part III. Field Experiment and Comparison with Theory," *J. Phys. Oceanogr.* **13**, 1505-1518, 1983.

Tang, S. and O.H. Shemdin, "Measurement of High Frequency Waves Using a Wave Follower," *J. Geophys. Res*. **88**, 4832-4840, 1983.

Thorpe, S.A. and P.N. Humphries, "Bubbles and Breaking Waves," *Nature* **283**, 463-465, 1980.

Toba, Y., "Stochastic Form of the Growth of Wind Waves in a Single-parameter Representation with Physical Implications," *J. Phys. Oceanogr.* **8**, 494-507, 1978.

Valenzuela, G.R., "Theories for the Interaction of Electromagnetic and Oceanic Waves - A Review," *Bound-Layer Meteorol.* **13**, 61-85, 1978.

Witter, D.L. and D.B. Chelton, "A Geosat Altimeter Wind Speed Algorithm and a Method for Altimeter Wind Speed Algorithm Development," *J. Geophys. Res.* **96**, 8853-8860, 1991.

Wu, J., "Sea-surface Slope and Equilibrium Wind-Wave Spectra," *Phys. Fluids* **15**, 741-746, 1972.

Wu, J., "Oceanic Whitecaps and Sea State," *J. Phys. Oceanogr.* **9**, 1064-1068, 1979.

Wu, J., "Near-nadir Microwave Specular Returns from the Sea Surface - Altimeter Algorithms for Wind Speed and Wind Stress," *J. Atm. Ocean. Tech.* **9**, 659-667, 1992.

Zheng, Q.A., V. Klemas, G.S. Hyane, and N.E. Huang, "The Effect of Oceanic Whitecaps and Foams on Pulse-limited Radar Altimeters," *J. Geophys. Res.* **88**, 2571-2578, 1983.